The PfRCR complex bridges malaria parasite and erythrocyte during invasion

https://doi.org/10.1038/s41586-023-06856-1

Received: 30 January 2023

Accepted: 9 November 2023

Brendan Farrell[1,2], Nawsad Alam[1,2,4], Melissa N. Hart[3,4], Abhishek Jamwal[1,2], Robert J. Ragotte[1,2], Hannah Walters-Morgan[1,2], Simon J. Draper[1,2], Ellen Knuepfer[3] & Matthew K. Higgins[1,2] ✉

The symptoms of malaria occur during the blood stage of infection, when parasites invade and replicate within human erythrocytes. The PfPCRCR complex[1], containing PfRH5 (refs. 2,3), PfCyRPA, PfRIPR, PfCSS and PfPTRAMP, is essential for erythrocyte invasion by the deadliest human malaria parasite, *Plasmodium falciparum*. Invasion can be prevented by antibodies[3–6] or nanobodies[1] against each of these conserved proteins, making them the leading blood-stage malaria vaccine candidates. However, little is known about how PfPCRCR functions during invasion. Here we present the structure of the PfRCR complex[7,8], containing PfRH5, PfCyRPA and PfRIPR, determined by cryogenic-electron microscopy. We test the hypothesis that PfRH5 opens to insert into the membrane[9], instead showing that a rigid, disulfide-locked PfRH5 can mediate efficient erythrocyte invasion. We show, through modelling and an erythrocyte-binding assay, that PfCyRPA-binding antibodies[5] neutralize invasion through a steric mechanism. We determine the structure of PfRIPR, showing that it consists of an ordered, multidomain core flexibly linked to an elongated tail. We also show that the elongated tail of PfRIPR, which is the target of growth-neutralizing antibodies[6], binds to the PfCSS–PfPTRAMP complex on the parasite membrane. A modular PfRIPR is therefore linked to the merozoite membrane through an elongated tail, and its structured core presents PfCyRPA and PfRH5 to interact with erythrocyte receptors. This provides fresh insight into the molecular mechanism of erythrocyte invasion and opens the way to new approaches in rational vaccine design.

Erythrocyte invasion by *Plasmodium falciparum* involves a tightly ordered sequence of events, starting when the merozoite form of the parasite contacts an erythrocyte[10,11]. This is followed by both a strong, actin-dependent deformation of the erythrocyte surface and reorientation of the merozoite to place its apical pole adjacent to the erythrocyte membrane. Discharge of apical organelles releases the machinery required for invasion, including the PfRCR complex. This leads to both a calcium spike at the merozoite–erythrocyte contact site and the formation of a moving junction between the merozoite and erythrocyte. The parasite then actively pulls its way inside the erythrocyte, followed immediately by a series of deformations of the infected erythrocyte and the establishment of the parasite inside a vacuole.

These stages of erythrocyte invasion require multiple host–parasite interactions, many of which are mediated by protein families with redundant functions[10]. However, no strain of *P. falciparum* has yet been found that can invade erythrocytes when the interaction between PfRH5 (refs. 12,13) and membrane complexes containing the erythrocyte receptor basigin[14,15] is prevented. Indeed, both PfRH5 and basigin are targets of invasion-neutralizing antibodies[4,14,16,17], and immunization with PfRH5 is protective in an *Aotus* model of malaria[12] and delays the onset of symptoms in a human challenge model[13]. PfRH5 assembles with PfCyRPA and PfRIPR to form the tripartite PfRCR complex[7,8,18]. Both PfCyRPA and PfRIPR are also essential for erythrocyte invasion and are targets of invasion-blocking antibodies[5–7,19–21]. More recently a complex containing two merozoite surface proteins, PfCSS and PfPTRAMP, has been shown to bind to PfRCR and the structure of PfCSS was determined[1]. That RIPR, CSS and PTRAMP interact together was first identified in *Plasmodium knowlesi*, in which these proteins are also essential for invasion[22]. Invasion-neutralizing nanobodies have been identified against both PfCSS and PfPTRAMP[1], and all five members of PfPCRCR are potential components of a blood-stage malaria vaccine.

Despite the essential function of each component of the PfRCR complex, their roles during invasion are enigmatic. Blocking the function of any member of PfPCRCR halts invasion of erythrocytes at the same step within the invasion process, preventing increase in calcium concentration at the parasite–erythrocyte interface, an event thought to occur before moving junction formation[1]. Several models for PfRH5 function have been proposed, including one that suggests that PfRH5 and PfRIPR undergo substantial conformational changes to insert into the erythrocyte membrane, forming pores[9], and another that suggests that PfRH5 modulates signalling pathways leading to cytoskeletal changes during invasion[23]. However, neither of these hypotheses is robustly supported. To further understand the role of PfRCR in

---

[1]Department of Biochemistry, University of Oxford, Oxford, UK. [2]Kavli Institute for Nanoscience Discovery, University of Oxford, Oxford, UK. [3]The Royal Veterinary College, Hatfield, UK. [4]These authors contributed equally: Nawsad Alam, Melissa N. Hart. ✉e-mail: matthew.higgins@bioch.ox.ac.uk

invasion, we therefore determined its structure at 3.0 Å resolution using cryogenic-electron microscopy (cryo-EM) and assessed the role of PfRH5 and PfRIPR in invasion.

Structure of the PfRCR complex

Although crystal structures are available for both PfRH5 (refs. 3,4) and PfCyRPA[5], structural information for PfRCR is limited to a cryo-EM map of the complex at around 7 Å resolution[9]. Higher resolution was not achieved in this previous study because the PfRCR complex adopted preferred orientations when vitrified, preventing uniform imaging and reducing the resolution of the subsequent three-dimensional reconstruction. Crystal structures of PfRH5 and PfCyRPA could be docked into this map, providing insight into the architecture of PfRCR, but this yielded neither atomic-level information on the structure of PfRIPR nor the interactions among the PfRCR components. To provide an atomic resolution model of PfRCR we assessed the ability of Fab fragments from monoclonal antibodies, which bind to PfRH5 or PfCyRPA, to reduce the likelihood of PfRCR adopting preferred orientations. A complex of PfRCR bound to the Fab fragment of the invasion-neutralizing anti-PfCyRPA antibody Cy.003 (ref. 5) (Extended Data Fig. 1a,b) had a sufficiently uniform particle distribution to generate a consensus cryo-EM map with a global resolution of 3.0 Å (Fig. 1a, Extended Data Figs. 1c,d and 2 and Extended Data Table 1).

Crystal structures of PfRH5 (ref. 3) and the PfCyRPA–Cy.003 Fab complex[5] were docked into this map, confirming that PfCyRPA lies at the centre of PfRCR, bridging PfRH5 and PfRIPR (Fig. 1). This arrangement is also consistent with chemical crosslinks observed in crosslinking mass spectrometry (XL-MS) analysis of the PfRCR complex (Extended Data Fig. 3 and Extended Data Table 2). The region of electron density attributed to PfRIPR in this consensus map was not sufficiently large to accommodate the full-length molecule, suggesting that part of PfRIPR is flexibly attached to the ordered part of PfRCR, and was therefore not resolved. Local-resolution estimation indicated that PfCyRPA–Cy.003 was best resolved in the consensus map and PfRIPR the least well, especially at its PfCyRPA-distal edge (Fig. 1a).

To investigate the cause of the lower local resolution of PfRIPR, and to identify ways to improve map quality, we subjected particles of the PfRCR–Cy.003 complex to three-dimensional variability analysis in cryoSPARC[24], showing conformational heterogeneity (Supplementary Video 1). Flexibility was observed along the length of PfRCR, with both PfRH5 and PfRIPR rocking relative to PfCyRPA and with further internal motion observed within PfRIPR, both consistent with observed local-resolution estimates (Fig. 1a). We therefore performed local refinement of both PfRH5 and PfRIPR, significantly improving the density for PfRIPR (Extended Data Figs. 1e and 2). A composite map generated by combining these global and local refinements was used to build a model of PfRCR (Fig. 1b and Extended Data Table 1). Chemical crosslinks identified through XL-MS analysis of the PfRCR complex are consistent with this model (Extended Data Fig. 3 and Extended Data Table 2).

Despite isolation of an intact PfRCR–Cy.003 complex by gel filtration (Extended Data Fig. 1a,b), ab initio reconstructions showed that a second complex lacking PfRH5 was also present in the dataset (Extended Data Fig. 2). This was separately refined yielding a consensus map with a global resolution of 3.1 Å (Extended Data Fig. 1f–h). The map of this PfCyRPA–PfRIPR–Cy.003 complex also showed lower local resolution at the region corresponding to PfRIPR (Extended Data Fig. 1f), again consistent with the flexibility observed in three-dimensional variability analysis. We therefore built a model of this PfCyRPA–PfRIPR–Cy.003 complex using a composite map from consensus and local refinements (Extended Data Fig. 4a and Extended Data Table 3).

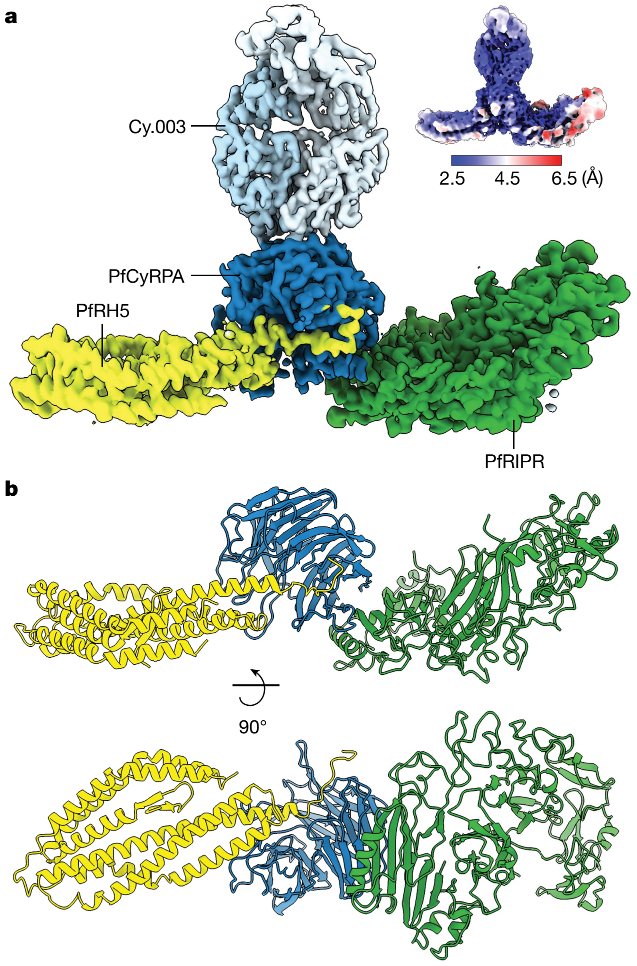

Fig. 1 | Structure of the PfRCR complex. a, Composite map of the PfRCR–Cy.003 complex, following local refinement of the consensus map and postprocessing with DeepEMhancer. Densities corresponding to PfRH5 (yellow), PfCyRPA (dark blue), PfRIPR (green) and Cy.003 (light blue) are highlighted. Inset at top right is the unsharpened consensus map before local refinement, coloured by local resolution. **b**, Structure of the PfRCR complex in cartoon representation, coloured as in **a**. Cy.003 is omitted for clarity.

Dynamics at the PfRH5–PfCyRPA interface

To understand the interface between PfCyRPA and PfRH5 we first assessed the structure of PfRCR–Cy.003, comparing it with the crystal structures of PfRH5 and PfCyRPA—either free or in complex with ligands or antibodies (Fig. 2a,b and Extended Data Fig. 4). PfCyRPA and PfRH5 each have a buried surface area of approximately 1,720 Å^2 with binding mediated by salt bridges, hydrogen bonds and hydrophobic interactions (Extended Data Table 4). No global conformational changes were observed in PfRH5 when compared with unbound PfRH5, with much of the PfRH5–PfCyRPA interface formed through rigid-body docking of blades 3 and 4 of the PfCyRPA β-propeller against helices α5 and α7 of PfRH5 (Fig. 2a). PfRH5 helix α7 projects towards the centre of the β-propeller of PfCyRPA, and the most substantial change observed in PfRH5 following PfCyRPA binding was an ordering of its C-terminal tail (residues 507–516). These residues follow α7 and were disordered in previous structures. In PfRCR these adopt an elongated conformation and occupy a groove that passes between blades 1 and 6 of PfCyRPA, pointing towards, but not contacting, PfRIPR.

A more substantial conformational change is observed in PfCyRPA when present in the PfRCR complex (Fig. 2b). Whereas blades 1–4 overlay closely with those in the crystal structures of PfCyRPA (root

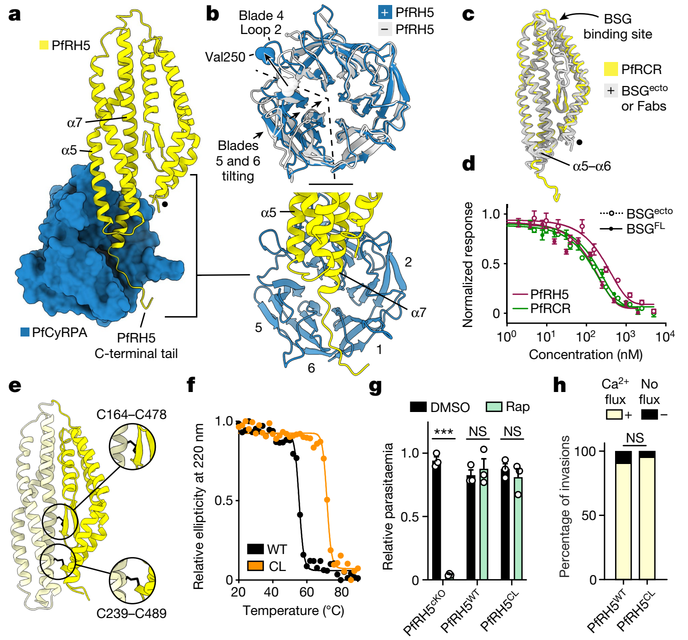

Fig. 2 | PfRH5 is a rigid component of PfRCR that does not open during invasion. a, The interface between PfRH5 (yellow cartoon) and PfCyRPA (blue surface). PfCyRPA blade 1 corresponds to Ile49–Lys95. The internal α2–α3 loop of PfRH5, unresolved in these data, is indicated by a black dot. Inset lower right, the interface between PfRH5 and PfCyRPA, with the blades of PfCyRPA labelled. **b**, Overlay of PfCyRPA from PfRCR–Cy.003- (blue) and Cy.003-bound PfCyRPA (grey; PDB: 7PI2)[5], showing changes induced by PfRH5 binding. Val250 is shown as spheres. **c**, Overlay of PfRH5 from PfRCR–Cy.003 (yellow) and previous structures of PfRH5 bound to either BSG^{ecto} (PDB: 4U0Q)[3] or anti-PfRH5 Fab fragments (PDBs: 4U0R, 4U1G, 6RCU, 6RCV and 7PHU)[3–5] (grey). **d**, Microscale thermophoresis responses showing equivalent binding of BSG^{ecto} (dotted lines) and BSG^{FL} (full lines) to PfRH5 (maroon) and PfRCR (green); $n = 2$ biologically independent samples (one shown), both measured in triplicate. Mean plus or minus s.d. is shown. **e**, Model of the designed PfRH5^{CL} and its disulfide bonds (black), which lock together N-PfRH5 (dark yellow) and C-PfRH5 (light yellow). **f**, PfRH5^{CL} (orange) shows improved thermal stability compared with PfRH5^{WT} (black), as measured by circular dichroism. **g**, Conditional rapamycin (Rap)-induced knockout of PfRH5 (PfRH5^{cKO}) reduced parasitaemia (***$P < 0.001$) but replacement with PfRH5^{WT} or PfRH5^{CL} did not ($P = 0.599$ and $P = 0.457$, respectively, two-tailed unpaired *t*-test); $n = 3$ biologically independent samples, each measured in triplicate. Mean plus or minus s.e.m. is shown. **h**, Percentage of invasion events by WT or PfRH5^{CL} parasites, showing a calcium flux (yellow) or no flux (black). No significant difference was observed ($P = 0.68$, two-tailed Fisher's exact test); $n = 41$ invasion events for both PfRH5^{WT} and PfRH5^{CL} parasites from three biological replicates. NS, not significant.

mean squared deviation (r.m.s.d.) 0.63 Å for Cy.003-bound PfCyRPA and 0.66 Å for unbound PfCyRPA (Fig. 2b and Extended Data Fig. 4b)), blades 5 and 6 and the linker between them move closer to the central axis of its β-propeller when in PfRCR, predominantly through a rigid-body tilt. This alters the width of the groove in which lie residues 507–516 of PfRH5. This is accompanied by a substantial and more localized rearrangement in loop 2 of blade 4, which moves by 11.5 Å at Val250 to accommodate helix α5 of PfRH5, with additional changes to loop 2 of each of blades 1–3 and to the linker between blades 3 and 4. To determine whether these changes were induced by PfRH5 binding, we compared the structure of PfCyRPA in PfRCR–Cy.003 with that in the PfCyRPA–PfRIPR–Cy.003 complex (Extended Data Fig. 4b). In this latter complex, PfCyRPA adopts a structure more like that observed in crystal structures (with r.m.s.d. of 0.63 Å for Cy.003-bound PfCyRPA and 0.62 Å for unbound PfCyRPA, versus 0.86 Å for PfCyRPA in PfRCR–Cy.003), indicating that these conformational changes are the result of PfRH5 binding. Notably, in both PfRH5 and PfCyRPA, the epitopes previously found to be the targets of neutralizing antibodies[3–5] do not change in conformation following complex formation, supporting vaccine immunogen design approaches based on original crystal structures.

PfRCR retains PfRH5 fold and function

Previous studies have suggested that PfRH5 is flexible, that its binding to basigin is influenced by its assembly into the PfRCR complex and that the N- and C-terminal halves of PfRH5 open to allow it to insert into the erythrocyte membrane to form a pore[9]. To test these hypotheses we started by assessing whether the structure of PfRH5 from our PfRCR–Cy.003 complex is different from previously determined PfRH5 structures. The global rigid-body motions along the length of the PfRCR complex (Supplementary Video 1) result in the distal tips of PfRCR appearing lower in resolution in the consensus PfRCR–Cy.003 cryo-EM map than the core of the complex (Fig. 1a). However, we hypothesized that this was an artefact of single-particle averaging for a flexible molecular assembly. Indeed, following local refinement to partially correct this flexibility, we found that the PfCyRPA-distal tip of PfRH5 in our locally refined map had a local resolution of about 4–5 Å, with higher resolution within its core (Extended Data Fig. 4c). This improved resolution of PfRH5 in the PfRCR complex allowed us to dock and refine a molecular model of PfRH5 more reliably (Extended Data Fig. 4d). Comparison of this refined model with the crystal structures of PfRH5, bound either to basigin[3] or to monoclonal Fab fragments[3–5], showed no consistent conformational changes in PfRH5 as a result of being part of PfRCR (with r.m.s.d. for each of less than 1 Å; Fig. 2c and Extended Data Fig. 4e). The only variable regions of PfRH5 across this alignment are the loop-linking helices α5 and α6 and the C-terminal end of α7, which are both within the region of PfRH5 that contacts PfCyRPA. The PfCyRPA-bound conformation is not an outlier when compared with other PfRH5 structures, suggesting that these are intrinsically flexible regions of PfRH5 that become ordered on binding to PfCyRPA. We therefore observed no conformational change in PfRH5 induced by assembly into PfRCR.

The finding that PfRH5 adopts a similar conformation in PfRCR as when bound to basigin[3] led us to question a previous observation that PfRCR does not bind to the basigin ectodomain (BSG^{ecto})[9]. We therefore measured binding of PfRCR and PfRH5 to either BSG^{ecto} or detergent-solubilized full-length basigin (BSG^{FL}) using microscale thermophoresis (Fig. 2d and Extended Data Fig. 4f). Binding was observed in each case, with affinities ranging from around 0.12 µM for PfRH5 binding to full-length basigin to about 0.19 µM for PfRH5 binding to BSG^{ecto}, with the affinities for PfRCR binding to either form of basigin falling between these values (Extended Data Fig. 4f). We therefore find that PfRCR and PfRH5 bind to both basigin and its ectodomain with similar affinity, not supporting the hypothesis that assembly into the PfRCR complex changes the basigin-binding properties of PfRH5. Together with structure comparisons, these data show that assembly into the PfRCR complex does not affect the structure of PfRH5, nor its ability to bind to basigin.

PfRH5 does not disassemble into a pore

Our structural studies do not rule out the possibility that the N- and C-terminal halves of PfRH5 might come apart during the erythrocyte invasion process, allowing PfRH5 to form a pore that causes a spike in calcium concentration at the merozoite–erythrocyte interface[9]. We therefore directly tested pore formation using a previously described haemolysis assay. In contrast to a previous study[9], we observed no significant haemolysis in the presence of PfRH5, PfRIPR or PfRCR whereas alpha-haemolysin, a pore-forming toxin, caused considerable haemolysis (Extended Data Fig. 4g). Moreover, we did not observe an increase in calcium concentration within red blood cells following their incubation with PfRH5 or PfRCR (Extended Data Fig. 4h,i), which was described previously[21]. Having observed no evidence of pore formation in these in vitro assays, we next developed a parasite-based assay in which we introduced locking disulfide bonds into the centre of PfRH5 that would prevent the separation of its N- and C-terminal halves, and used a conditional replacement system to introduce these into a *P. falciparum* line to assess their effect on erythrocyte invasion (Fig. 2e–h). We employed a Rosetta[25]-based, structure-guided approach to design five disulfide bonds that we predicted would hold together the N- and C-terminal halves of PfRH5 (Cys164–Cys478 (CC1), Cys180–Cys471 (CC2), Cys300–Cys408 (CC3), Cys166–Cys481 (CC4) and Cys239–Cys489 (CC5)) (Extended Data Fig. 5a). In each case these were introduced into a version of PfRH5 lacking the N terminus and disordered loop (PfRH5ΔNL)[3], were expressed in *Drosophila* S2 cells and were shown by circular dichroism analysis to adopt the expected secondary structure (Extended Data Fig. 5b–d). We used circular dichroism with a thermal melt to test the stability of these five variants and found that two of the designed disulfide bonds increased the thermal stability of PfRH5ΔNL by over 5 °C, as would be expected following successful formation of a stabilizing disulfide bond (+6 °C for CC1 and +8 °C for CC5; Extended Data Fig. 5e). These two disulfide bonds were then combined to generate a final cysteine-locked PfRH5 design (PfRH5$^{\text{CL}}$; Fig. 2e and Extended Data Fig. 5c,f) and this combination increased the thermal stability of PfRH5ΔNL by around 14 °C, indicating that both designed cysteine locks had been formed (Fig. 2f). We further validated the presence of these disulfide bonds in PfRH5$^{\text{CL}}$ by mass spectrometry analysis following maleimide-PEG2-biotin labelling[26], which modifies free sulfhydryl groups but not disulfide-bonded cysteine residues. Non-reduced PfRH5ΔNL$^{\text{CL}}$ was modified by the addition of just one maleimide, indicating that it contains only one free cysteine, most probably corresponding to the native single free cysteine, Cys239 (Extended Data Fig. 5g). By contrast, reduced PfRH5ΔNL$^{\text{CL}}$ showed a series of species following labelling, containing from zero to eight maleimide modifications, consistent with a total of nine cysteine residues and partial labelling. Taken together, these data confirm that PfRH5$^{\text{CL}}$ contains four disulfide bonds (two native and two designed) that are formed under non-reducing conditions.

We next generated a transgenic *P. falciparum* line that could be used to induce a conditional replacement of the native PfRH5 gene with the cysteine-locked variant (Extended Data Fig. 6). To achieve this, *LoxP* sites were inserted silently within a synthetic intron[27] either side of exon 2 of the endogenous PfRH5 gene, generating a conditional knockout line (PfRH5$^{\text{cKO}}$) in which the addition of rapamycin would lead to excision of the coding sequence of the gene (Extended Data Fig. 6a). Two further strains were then generated in which a second copy of PfRH5 (either a wild-type (WT) sequence, PfRH5$^{\text{WT}}$, or the cysteine-locked variant, PfRH5$^{\text{CL}}$) was inserted downstream of the endogenous floxed PfRH5 gene such that the addition of rapamycin would lead to removal of the endogenous PfRH5 sequence and expression of the downstream copy (Extended Data Fig. 6b–e). We then tested the ability of all three lines to invade erythrocytes by treating ring-stage parasites with rapamycin or dimethylsulfoxide (DMSO) as a control, then measuring their resultant parasitaemia (Fig. 2g). The addition of rapamycin to PfRH5$^{\text{cKO}}$, which lacks a downstream replacement copy of PfRH5, led to a reduction of over 95% in parasitaemia, confirming the requirement of PfRH5 for invasion. However, in parasite lines with a downstream copy of either PfRH5$^{\text{WT}}$ or PfRH5$^{\text{CL}}$ the addition of rapamycin did not affect parasitaemia, demonstrating that both were able to complement the deletion of PfRH5 and facilitate effective erythrocyte invasion. We next assessed whether the calcium flux that occurs at the merozoite–erythrocyte junction is also observed when PfRH5 is cysteine locked, and found no significant difference between the fraction of cells in which a calcium flux was observed during invasion events when comparing PfRH5$^{\text{WT}}$ and PfRH5$^{\text{CL}}$ lines (Fig. 2h and Supplementary Videos 2 and 3). The ability of a PfRH5 variant that is locked through two disulfide bonds across its N- and C-halves to mediate invasion is not compatible with a model in which the PfRH5 structure is required to 'open' such that it can insert into the erythrocyte membrane. Instead, this is consistent with PfRH5 adopting a rigid structure throughout the process of erythrocyte invasion with the calcium flux, which occurs downstream of PfRH5, not resulting from a PfRH5-mediated pore.

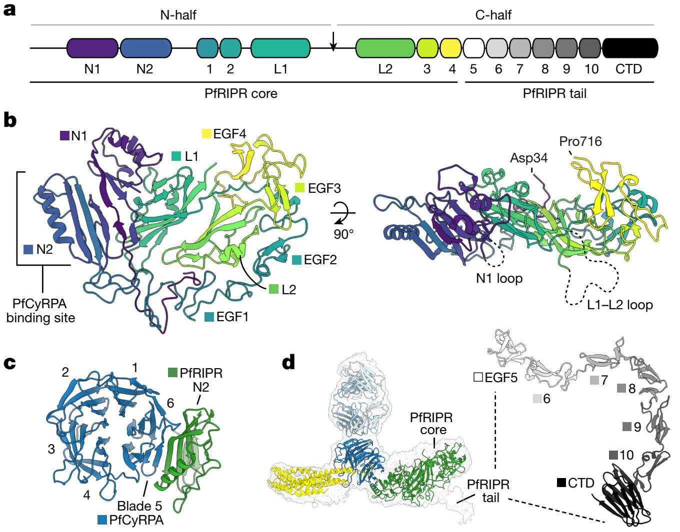

Fig. 3 | The structure of PfRIPR. a, The domain architecture of PfRIPR. The PfRIPR core comprises the N terminus to EGF-like domain 4, and its tail comprises EGF-like domain 5 to the C terminus. In addition to the ten previously known EGF-like domains, PfRIPR contains two N-terminal domains (N1 and N2), two lectin-like domains (L1 and L2) and a CTD. PfRIPR is cleaved at a site in the L1–L2 loop to produce its N- and C-halves, indicated by an arrow. **b**, Structure of the PfRIPR core (residues Asp34–Pro716) coloured sequentially from its N terminus (blue) to C terminus (yellow), as in **a**. The location of the PfCyRPA-binding site on domain N2, and the unresolved N1 loop (residues 124–137) and L1–L2 loop (residues 479–557), are shown. **c**, A view of the interface between PfCyRPA and PfRIPR, illustrating the extended β-sheet between PfCyRPA blade 5 and PfRIPR domain N2, plus some interactions with the helix of N2. Only domain N2 of PfRIPR is shown, for clarity. **d**, The 4.0 Å unsharpened map of the PfRCR–Cy.003 complex containing additional density for the beginning of the PfRIPR tail. The AlphaFold2 prediction of the PfRIPR tail is shown (right), with EGF-like domains and the CTD labelled and coloured in greyscale as in **a**.

The structure of PfRIPR

We next used our composite cryo-EM map of PfRCR–Cy.003 to build a molecular model of PfRIPR (Fig. 3). Map resolution was sufficient to build much of the structure de novo (Extended Data Fig. 7a), with molecular models derived from structure prediction, including those from a local installation of AlphaFold2 (ref. 28), used to guide building (Extended Data Fig. 7b), particularly in the less well-ordered regions of the map. This resulted in an almost complete model of residues 34–716 of PfRIPR (which has a total length of 1,086 residues), with no density observed for loops comprising residues 124–137 and 479–557 (Fig. 3). Moreover, we did not observe any interpretable density for residues 717–1,086 of PfRIPR, showing that this C-terminal region of PfRIPR is flexibly connected to the PfRCR complex. This is consistent with the internal crosslinks found within PfRIPR from XL-MS analysis of PfRCR, most of which were in the first 700 or so residues (Extended Data Fig. 3).

The structure of PfRIPR allowed us to redefine its domain architecture (Fig. 3a,b). PfRIPR has previously been described as consisting of two halves generated by cleavage of PfRIPRP[29], with these halves remaining associated[7]. Through sequence analysis, PfRIPR was also predicted to contain ten epidermal growth factor (EGF)-like domains, with two in the N-half (EGF1 and EGF2) and eight in the C-half (EGF3–EGF10)[7]. In our PfRIPR structure, the predicted cleavage site that joins the two predicted halves of PfRIPR is found within a large unstructured loop (residues 479–557). However, this loop does not link two separate halves of PfRIPR but instead emerges from within an ordered array of different domains, which ends after domain EGF4. We call this region the PfRIPR core.

The core of PfRIPR adopts a complex new architecture in which eight domains are intertwined (Fig. 3b). The two N-terminal domains, N1 and N2, each consist of a three- or four-stranded β-sheet packing against one or two α-helices. These two domains interact with one another through their β-sheets and it is through domain N2 that PfRIPR binds to PfCyRPA, with the three-stranded β-sheet of N2 forming a continuation of the β-sheet of PfCyRPA blade 5 (Fig. 3c). The interface between PfRIPR and PfCyRPA has a total buried surface area of roughly 1,060 Å^2, formed predominantly through hydrophilic side chains, with contacts also being made between the long α-helix of N2 and the face of PfCyRPA blade 5, and between domain N1 and the N-terminal β-strand of PfCyRPA, which is found in blade 6 (Extended Data Fig. 7c and Extended Data Table 4). After a short sequence following N2, the first two EGF-like domains of PfRIPR, EGF1 and EGF2 follow, wrapping around one edge of the core. Next are two domains, L1 and L2, which form the centre of the PfRIPR core and around which the other domains fold. Intriguingly, L1 and L2 adopt the same fold as rhamnose-binding lectins and therefore the same fold as PfP113 (ref. 30) (Extended Data Fig. 7d), a proposed binding partner of PfRH5 that was previously thought to anchor PfRH5 to the merozoite surface[31] but which was recently disputed as a surface protein[32]. The large disordered internal loop where PfRIPR is cleaved links L1 and L2. Multiple interdomain contacts within the PfRIPR core, including those between L1 and L2, hold the N- and C-halves of PfRIPR together following loop cleavage. Finally, EGF3 and EGF4 pack against the linker that joins EGF2 and L1, wrapping around the opposite edge of the PfRIPR core. This leaves the C terminus of the PfRIPR core at the side opposite to the PfCyRPA-binding site, and on the opposing face to N1 and the L1–L2 loop. Whereas the PfRIPR core is cysteine rich, containing 23 disulfide bonds and one free cysteine (Cys256), these are all contained within domains and there are no interdomain disulfide bonds (Extended Data Fig. 7e).

Whereas the map of PfRCR–Cy.003 did not contain density of sufficient resolution to allow model building of PfRIPR beyond residue 716, in several two-dimensional classes we could see weaker additional density projecting away from the PfRIPR core (Extended Data Fig. 2). This density could not be improved or extended using two-dimensional classification with a larger particle box size, suggesting that it results from residues flexibly linked to the PfRIPR core. Nonetheless, non-uniform refinement of a subset of particles yielded a map at a global resolution of 4.0 Å (Fig. 3d and Extended Data Fig. 7f), which showed that this extra density projects away from the centre of the PfRIPR core, adjacent to where EGF4 ends at residue 716. This suggested that the remainder of PfRIPR extends away from the PfRIPR core at this location. Indeed, XL-MS analysis identified a crosslink between Lys736 of EGF5 and Lys427 of domain L1, indicating that EGF5 is located approximately in this area (Extended Data Fig. 3 and Extended Data Table 2) and as supported by an AlphaFold2 prediction of PfRIPR up to the end of EGF5 (Extended Data Fig. 7g). To generate a complete composite model of full-length PfRIPR we used AlphaFold2 to predict the structure of residues 717–1,086 of PfRIPR. This predicts an elongated but ordered structure that we call the PfRIPR tail, consisting of EGF-like domains 5–10 followed by a C-terminal domain (CTD) with a galectin-like fold (Fig. 3d and Extended Data Fig. 7d). Guided by the additional density in the 4.0 Å map, we docked this model of the PfRIPR tail onto the PfRIPR core to generate a complete molecular model for PfRIPR (Extended Data Fig. 7h).

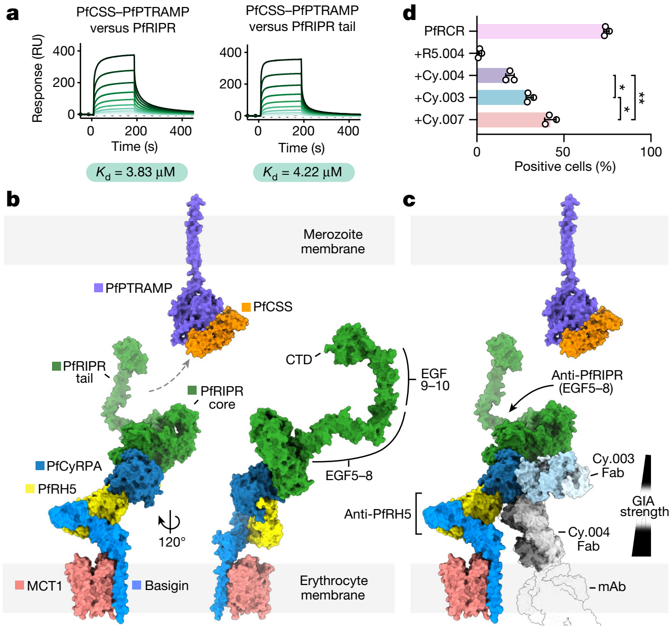

Fig. 4 | The PfPCRCR complex bridges the parasite and erythrocyte membranes. a, The PfCSS–PfPTRAMP complex binds to full-length PfRIPR and its tail with equal affinity, as measured by surface plasmon resonance; $n = 4$ independent experiments (one shown). RU, response units. The binding affinity given is the mean of those determined by steady-state analysis of each independent measurement (Extended Data Fig. 8d). **b**, Composite model of the PfRCR complex on the erythrocyte membrane, illustrating how the tail of PfRIPR projects towards the merozoite membrane where PfCSS–PfPTRAMP is located. EGF-like domains 5–8 and 9–10 and the CTD of PfRIPR are highlighted. The composite PfRCR complex model is aligned onto the structure of basigin-bound MCT1 (PDB: 7CKR[33]). For illustrative purposes only, the AlphaFold2-predicted structure of PfPTRAMP (magenta, AlphaFoldDB: Q8I5M8, residues 26–352) and the crystal structure of PfCSS (orange, PDB: 7UNY[1]) are docked together. **c**, Mapping of growth-inhibitory antibodies targeting PfRCR components in the context of erythrocyte binding. The potency of growth-inhibitory PfCyRPA-targeting antibodies correlates with their proximity to the erythrocyte membrane, illustrated by overlay of Cy.004 Fab-bound PfCyRPA (PDB: 7PHW[5]) onto PfRCR–Cy.003. The approximate location of the Fc portion of the intact monoclonal antibody is shown as a faint silhouette through overlay of the crystal structure of an intact antibody (PDB: 1IGT). Growth-inhibitory PfRIPR-targeting antibodies bind to EGF-like domains 5–8, located distal to the erythrocyte membrane. **d**, The ability of PfRCR to bind to human erythrocytes, either alone or in the presence of twofold molar excess of antibodies R5.004, Cy.003, Cy.004 and Cy.007, expressed as a percentage of PfRCR-positive cells; $n = 3$ independent measurements; mean plus or minus s.d. is shown; $P = 0.0132$ for Cy.003 versus Cy.004, $P = 0.0418$ for Cy.003 versus Cy.007 and $P = 0.0023$ for Cy.004 versus Cy.007 (one-way Brown–Forsythe and Welch analysis of variance adjusted for multiple comparisons with Dunnett T3).

The PfRIPR tail binds PfCSS–PfPTRAMP

The *P. knowlesi* homologues of RIPR, PkRIPR and, more recently, PfRIPR itself have been shown to bind their respective homologues of the CSS–PTRAMP complex[1,22]. However, the binding interface between these proteins is undefined. We first confirmed that the PfCSS–PfPTRAMP heterodimer could assemble with the PfRCR complex into a five-component complex (Extended Data Fig. 8a,b). Given that our structure shows that PfRIPR comprises two distinct regions, we next asked whether it is the core or the tail of PfRIPR that mediates binding to PfCSS–PfPTRAMP. We immobilized full-length PfRIPR and the PfRIPR tail (Extended Data Fig. 8c) on two separate flow paths of a surface plasmon resonance chip then flowed the PfCSS–PfPTRAMP heterodimer over these surfaces. Both PfRIPR and its tail bound to

PfCSS–PfPTRAMP with a similar affinity of about 4 μM (Fig. 4a and Extended Data Fig. 8d), indicating that the PfRIPR tail alone is sufficient for binding to the transmembrane-anchored PfCSS–PfPTRAMP complex. This arrangement positions the complex containing the PfRIPR core, PfCyRPA and PfRH5 such that it can bind to receptors such as basigin on the erythrocyte surface.

Mechanisms of neutralizing antibodies

Invasion-neutralizing monoclonal antibodies have been identified against each of PfRH5, PfCyRPA and PfRIPR. To understand how these antibodies block the invasion process, we mapped their binding sites onto a model of PfRCR. Because erythrocyte basigin is found in a stable complex with either plasma membrane calcium transporters (PMCAs) or the monocarboxylate transporter (MCT1)[15], we combined our structure of PfRCR with that of the PfRH5–basigin complex[3] and with structures of basigin–MCT1 (ref. 33) and basigin–PMCA[34] to generate composite models of the PfRCR complex on the erythrocyte surface (Fig. 4b and Extended Data Fig. 8f,g). Whereas there will be some flexibility in the presentation of the PfRCR complex due to hinge movements in basigin, modelling predicts that PfRCR will project away from the erythrocyte surface, with PfRH5 closest to the erythrocyte and with the PfRIPR tail projecting towards the merozoite surface. This arrangement is consistent with surface plasmon resonance binding data (Fig. 4a), which indicates that the PfRIPR tail mediates binding to PfCSS–PfPTRAMP.

Neutralizing antibodies targeting PfRH5 and PfCyRPA are proposed to act by sterically blocking the approach of PfRCR to the erythrocyte membrane, preventing it from binding to basigin and any potentially unknown surface receptors[5,6]. Indeed, the most effective PfRH5-binding neutralizing antibodies block PfRH5 from binding to basigin–PMCA and basigin–MCT1 complexes[15]. There is no known erythrocyte-binding partner for PfCyRPA, and the mechanism by which invasion-blocking, anti-PfCyRPA antibodies act is uncertain. Here we find that, when aligned onto the composite model of PfRCR–basigin–MCT1 and PfRCR–basigin–PMCA, the degree to which these antibodies project towards the erythrocyte membrane correlates with their growth-inhibitory activity[5] (Fig. 4c and Extended Data Fig. 8f,g). Aligning the crystal structure of PfCyRPA bound to the strongly neutralizing antibody Cy.004 (ref. 5) onto PfRCR places the Fab fragment of Cy.004 projecting towards the erythrocyte surface, where it would sterically clash with the membrane when part of an intact monoclonal antibody. By contrast, the less-neutralizing antibodies Cy.003, Cy.007, 8A7 and c12 project towards the erythrocyte membrane to a lesser degree. The invasion-blocking activity of these antibodies[5] thus correlates with the degree to which they project towards the erythrocyte membrane.

To test the hypothesis that PfCyRPA-binding antibodies sterically block binding of PfRCR to erythrocytes, we developed a flow cytometry-based assay. To detect binding of PfRCR to erythrocytes we first used a fluorescently labelled anti-C-tag nanobody that targets the affinity purification tag of the complex (Supplementary Fig. 2a,b). We observed that PfRCR bound to human erythrocytes and that the anti-PfRH5 neutralizing antibody R5.004 (ref. 4) blocked this binding but that the non-neutralizing antibody R5.011 (ref. 4) did not (Extended Data Fig. 8e). We therefore used R5.011 as the primary detection antibody in a second round of flow cytometry measurements, allowing signal amplification (Supplementary Fig. 2c). Here, following incubation of erythrocytes with PfRCR, we observed that around 74% of these were positively labelled (Fig. 4d). As before, R5.004, which directly prevents PfRH5 from binding to basigin[4], ablated erythrocyte binding. Each of the growth-neutralizing, PfCyRPA-targeting antibodies—Cy.003, Cy.004 and Cy.007 (ref. 5)—also reduced binding of PfRCR to erythrocytes (Fig. 4d and Supplementary Fig. 2d). Moreover, Cy.004, the most growth-neutralizing of these three antibodies[5], caused the greatest reduction in PfRCR binding, consistent with it projecting most directly towards the erythrocyte membrane as predicted from composite modelling (Fig. 4c). This supports a model in which PfCyRPA-targeting antibodies inhibit growth by sterically blocking the binding of PfRCR to the erythrocyte surface.

There are currently few studies detailing growth-inhibitory antibodies that target PfRIPR. The most effective known polyclonal and monoclonal antibodies targeting PfRIPR bind to EGF-like domains 5–8 in the PfRIPR tail[6,7,21]. How these antibodies block the invasion process will require further study but, because the tail of PfRIPR binds to PfCSS–PfPTRAMP, it is possible that they may affect processes such as receptor engagement on the merozoite surface rather than on the erythrocyte surface. Our knowledge of the structure of PfRIPR and how it assembles into the PfPCRCR complex will now allow future studies to assess the mechanisms of action of these PfRIPR tail-targeting antibodies. Future studies may also identify growth-inhibitory antibodies that bind the PfRIPR core, which have thus far been missed owing to small antibody panel sizes. Our structure will now enable a programme of structure-guided vaccine design based around PfRIPR to specifically induce and analyse such antibodies. For example, structure-guided approaches can be used to produce individual PfRIPR domains, resurfacing them to facilitate recombinant expression out of the context of the rest of PfRIPR. These could be used to raise antibodies towards specific regions of PfRIPR that may point towards the erythrocyte membrane, towards basigin or towards the PfCSS–PfPTRAMP complex on the merozoite surface. This will allow rational probing of the growth-neutralizing effects of antibodies targeting different surfaces of PfRIPR, showing its antigenic cartography and allowing rational design of immunogens that specifically elicit the most effective antibodies.

Conclusions

Our cryo-EM structure of PfRCR has allowed us to build an atomic model of PfRIPR, showing it to consist of a complex multidomain core flexibly attached to an elongated tail and containing domains that adopt the same fold as galectin- and rhamnose-binding lectins. We demonstrate the conformations of PfRH5, PfCyRPA and PfRIPR when part of PfRCR and define their interactions at the molecular level. We find that PfRH5 does not differ substantially in structure when integrated into the PfRCR complex, and that disulfide locking of the two halves of PfRH5 together has no impact on erythrocyte invasion, indicating that PfRH5 does not open to insert into the erythrocyte membrane as part of the invasion process. Calcium fluxes that occur during invasion are also unaffected by locking of PfRH5. Additionally, we find that the tail of PfRIPR binds to the PfCSS–PfPTRAMP complex, which is anchored at the merozoite surface, suggesting that PfRCR bridges both erythrocyte and parasite membranes during invasion. The mapping of growth-neutralizing antibodies onto the structure of erythrocyte-bound PfRCR supports a model in which antibodies that target PfRH5 and PfCyRPA sterically prevent PfRCR from binding to the erythrocyte membrane, which we confirm using a fluorescent activated cell sorting-based assay. By contrast, the most effective PfRIPR-targeting, invasion-neutralizing antibodies may act towards the parasite membrane. These studies inform and open new future avenues to understanding the molecular mechanisms of erythrocyte invasion and the rational design of blood-stage malaria vaccines.

Online content

Any methods, additional references, Nature Portfolio reporting summaries, source data, extended data, supplementary information, acknowledgements, peer review information; details of author contributions and competing interests; and statements of data and code availability are available at https://doi.org/10.1038/s41586-023-06856-1.

1. Scally, S. W. et al. PCRCR complex is essential for invasion of human erythrocytes by *Plasmodium falciparum*. *Nat. Microbiol.* **7**, 2039–2053 (2022).
2. Baum, J. et al. Reticulocyte-binding protein homologue 5 – an essential adhesin involved in invasion of human erythrocytes by *Plasmodium falciparum*. *Int. J. Parasitol.* **39**, 371–380 (2009).
3. Wright, K. E. et al. Structure of malaria invasion protein RH5 with erythrocyte basigin and blocking antibodies. *Nature* **515**, 427–430 (2014).
4. Alanine, D. G. W. et al. Human antibodies that slow erythrocyte invasion potentiate malaria-neutralizing antibodies. *Cell* **178**, 216–228 (2019).
5. Ragotte, R. J. et al. Heterotypic interactions drive antibody synergy against a malaria vaccine candidate. *Nat. Commun.* **13**, 933 (2022).
6. Healer, J. et al. Neutralising antibodies block the function of Rh5/Ripr/CyRPA complex during invasion of *Plasmodium falciparum* into human erythrocytes. *Cell. Microbiol.* **21**, e13030 (2019).
7. Chen, L. et al. An EGF-like protein forms a complex with PfRh5 and is required for invasion of human erythrocytes by *Plasmodium falciparum*. *PLoS Pathog.* **7**, e1002199 (2011).
8. Volz, J. C. et al. Essential role of the PfRh5/PfRipr/CyRPA complex during *Plasmodium falciparum* invasion of erythrocytes. *Cell Host Microbe* **20**, 60–71 (2016).
9. Wong, W. et al. Structure of *Plasmodium falciparum* Rh5-CyRPA-Ripr invasion complex. *Nature* **565**, 118–121 (2019).
10. Weiss, G. E. et al. Revealing the sequence and resulting cellular morphology of receptor-ligand interactions during *Plasmodium falciparum* invasion of erythrocytes. *PLoS Pathog.* **11**, e1004670 (2015).
11. Cowman, A. F., Tonkin, C. J., Tham, W. H. & Duraisingh, M. T. The molecular basis of erythrocyte invasion by malaria parasites. *Cell Host Microbe* **22**, 232–245 (2017).
12. Douglas, A. D. et al. A PfRH5-based vaccine is efficacious against heterologous strain blood-stage *Plasmodium falciparum* infection in *Aotus* monkeys. *Cell Host Microbe* **17**, 130–139 (2015).
13. Minassian, A. M. et al. Reduced blood-stage malaria growth and immune correlates in humans following RH5 vaccination. *Med* **2**, 701–719 (2021).
14. Crosnier, C. et al. Basigin is a receptor essential for erythrocyte invasion by *Plasmodium falciparum*. *Nature* **480**, 534–537 (2011).
15. Jamwal, A. et al. Erythrocyte invasion-neutralising antibodies prevent *Plasmodium falciparum* RH5 from binding to basigin-containing membrane protein complexes. *eLife* **5**, 12:e83681 (2023).
16. Douglas, A. D. et al. Neutralization of *Plasmodium falciparum* merozoites by antibodies against PfRH5. *J. Immunol.* **192**, 245–258 (2014).
17. Zenonos, Z. A. et al. Basigin is a druggable target for host-oriented antimalarial interventions. *J. Exp. Med.* **212**, 1145–1151 (2015).
18. Reddy, K. S. et al. Multiprotein complex between the GPI-anchored CyRPA with PfRH5 and PfRipr is crucial for *Plasmodium falciparum* erythrocyte invasion. *Proc. Natl Acad. Sci. USA* **112**, 1179–1184 (2015).
19. Chen, L. et al. Structural basis for inhibition of erythrocyte invasion by antibodies to *Plasmodium falciparum* protein CyRPA. *eLife* **6**, e21347 (2017).
20. Favuzza, P. et al. Structure of the malaria vaccine candidate antigen CyRPA and its complex with a parasite invasion inhibitory antibody. *eLife* **6**, e20383 (2017).
21. Nagaoka, H. et al. Antibodies against a short region of PfRipr inhibit *Plasmodium falciparum* merozoite invasion and PfRipr interaction with Rh5 and SEMA7A. *Sci. Rep.* **10**, 6573 (2020).
22. Knuepfer, E. et al. Divergent roles for the RH5 complex components, CyRPA and RIPR in human-infective malaria parasites. *PLoS Pathog.* **15**, e1007809 (2019).
23. Aniweh, Y. et al. *P. falciparum* RH5-Basigin interaction induces changes in the cytoskeleton of the host RBC. *Cell. Microbiol.* https://doi.org/10.1111/cmi.12747 (2017).
24. Punjani, A. & Fleet, D. J. 3D variability analysis: resolving continuous flexibility and discrete heterogeneity from single particle cryo-EM. *J. Struct. Biol.* **213**, 107702 (2021).
25. Leman, J. K. et al. Macromolecular modeling and design in Rosetta: recent methods and frameworks. *Nat. Methods* **17**, 665–680 (2020).
26. Robotham, A. C. & Kelly, J. F. Detection and quantification of free sulfhydryls in monoclonal antibodies using maleimide labeling and mass spectrometry. *mABs* **11**, 757–766 (2019).
27. Jones, M. L. et al. A versatile strategy for rapid conditional genome engineering using loxP sites in a small synthetic intron in *Plasmodium falciparum*. *Sci. Rep.* **6**, 21800 (2016).
28. Jumper, J. et al. Highly accurate protein structure prediction with AlphaFold. *Nature* **596**, 583–589 (2021).
29. Favuzza, P. et al. Dual plasmepsin-targeting antimalarial agents disrupt multiple stages of the malaria parasite life cycle. *Cell Host Microbe* **27**, 642–658 (2020).
30. Campeotto, I. et al. The structure of the cysteine-rich domain of *Plasmodium falciparum* P113 identifies the location of the RH5 binding site. *mBio* **11**, e01566-20 (2020).
31. Galaway, F. et al. P113 is a merozoite surface protein that binds the N terminus of *Plasmodium falciparum* RH5. *Nat. Commun.* **8**, 14333 (2017).
32. Bullen, H. E. et al. The *Plasmodium falciparum* parasitophorous vacuole protein P113 interacts with the parasite protein export machinery and maintains normal vacuole architecture. *Mol. Microbiol.* **117**, 1245–1262 (2022).
33. Wang, N. et al. Structural basis of human monocarboxylate transporter 1 inhibition by anti-cancer drug candidates. *Cell* **184**, 370–383 (2021).
34. Gong, D. et al. Structure of the human plasma membrane Ca(2+)-ATPase 1 in complex with its obligatory subunit neuroplastin. *Nat. Commun.* **9**, 3623 (2018).

Methods

Protein expression and purification

PfRH5 (residues E26–Q256, with substitutions C203Y (of the 7G8 *P. falciparum* strain) and T216A and T299A (to remove potential N-linked glycosylation sites), a BiP secretion sequence and a C-terminal C-tag), was expressed from a stable S2 cell line[35] (ExpreS^{2}ion Biotechnologies) in EX-CELL 420 Serum Free Medium (Sigma-Aldrich). After 3–4 days, culture supernatants were harvested and 0.45 µm filtered then incubated with CaptureSelect C-tagXL resin (Thermo Scientific). Beads were washed using 20–30 column volumes of Tris buffered saline (TBS) (25 mM Tris pH 7.5, 150 mM NaCl) and bound proteins eluted with C-tag elution buffer (25 mM Tris pH 7.5, 2 M $MgCl_2$). Eluted proteins were further purified by gel filtration using an S200 Increase 10/300 column with a running buffer of HEPES buffered saline (HBS) (20 mM HEPES pH 7.5, 150 mM NaCl). PfRH5ΔN[3] was also expressed from a stable S2 cell line and was purified as for full-length PfRH5 except that HBS containing 5% v/v glycerol was used as a running buffer for gel filtration.

PfCyRPA (residues D29–E362, with substitutions S147A, T324A and T340A (to remove potential N-linked glycosylation sites), a mammalian secretion sequence and a C-terminal C-tag) was transiently expressed using Expi293F cells with the Expi293 Expression System Kit (Thermo Fisher) as recommended by the manufacturer. Culture supernatants were harvested and 0.45 µm filtered, diluted 1:1 in TBS and then incubated with CaptureSelect C-tagXL resin. Purification then proceeded as for PfRH5.

PfRIPR (residues D21–N1086, with substitutions N103Q, N144Q, N228Q, N303Q, N334Q, N480Q, N498Q, N506Q, N526Q, N646Q, N647Q, N964Q and N1021Q (to remove potential N-linked glycosylation sites), a BiP secretion sequence and a C-terminal C-tag) was expressed from a stable S2 cell line as for PfRH5. After 3–4 days, culture supernatants were harvested and 0.45 µm filtered before being concentrated and buffer exchanged into 50 mM Tris pH 7.5 and 150 mM NaCl by tangential flow filtration with a stack of three 100 kDa Omega Cassettes (PALL Corporation). The exchanged supernatant was loaded onto a 1 ml prepacked CaptureSelect C-tagXL column (Thermo Scientific) equilibrated with TBS. Following washing with 30–50 column volumes of TBS, bound proteins were eluted with C-tag elution buffer. Eluted proteins were exchanged into HBS using a PD-10 desalting column (Cytiva) then either further purified by gel filtration as for PfRH5 or used directly for PfRCR complex preparation.

PfRIPR tail (residues D717–N1086, with substitutions N964Q and N1021Q (to remove potential N-linked glycosylation sites), a BiP secretion sequence and a C-terminal Avi-C-tag) was also expressed from a stable S2 cell line. PfRIPR tail was purified as for full-length PfRIPR except that filtered culture supernatants were exchanged into TBS by tangential flow filtration with a stack of three 5 kDa Omega Cassettes (PALL Corporation). Eluted proteins were further purified by gel filtration using an S200 Increase 10/300 column into HBS.

The PfCSS–PfPTRAMP heterodimer was obtained by coexpression of PfCSS (residues Q21–K290, with a secretion sequence and C-terminal His6-tag) and PfPTRAMP (residues C30–T307, with a secretion sequence and C-terminal His6-tag) using FreeStyle 293-F cells (Thermo Fisher) in FreeStyle F17 Expression Medium supplemented with L-glutamine and 1× MEM non-essential amino acids (Gibco). Six days following transfection, culture supernatants were harvested, 0.45 µm filtered then incubated with Super Ni-NTA resin (Generon) equilibrated in HBS. Following washing with 20 column volumes of HBS supplemented with 20 mM imidazole, bound proteins were eluted with HBS supplemented with 300 mM imidazole then further purified by gel filtration using an S200 Increase 10/300 column into HBS.

Cy.003, Cy.004, Cy.007 (ref. 5), R5.004 and R5.011 (ref. 4) were transiently expressed in Expi293F cells. Culture supernatants were harvested and 0.45 µm filtered before loading onto a 1 ml HiTrap Protein G HP column (Cytiva) pre-equilibrated in PBS (no. 79382, Sigma-Aldrich). The column was washed with PBS and bound proteins were eluted using 5 ml of 0.1 M glycine pH 2.5 into 1 ml of 1 M Tris pH 8.0. Eluted monoclonal antibodies (mAbs) were exchanged into PBS.

To prepare Fab fragments of Cy.003, the mAb was cleaved using Immobilized Papain (no. 20341, Thermo Scientific). Following cleavage, Fc and Fab fragments were separated using a 1 ml HiTrap rProtein A prepacked column (Cytiva) and the unbound fraction containing Cy.003 Fab was exchanged into PBS.

To express full-length human basigin, a synthetic gene (UniProt ID P35613-2) was cloned into pFastBac with a C-terminal His6-tag for expression in Sf9 insect cells using the Bac-to-Bac Baculovirus Expression System (Thermo Fisher). Following transformation of DH10Bac cells, bacmids were isolated by isopropanol precipitation and used to transfect Sf9 cells at a cell density of 1 million per ml in Sf-900 II serum-free medium (Gibco). First-generation baculoviruses (P1) were amplified to produce second-generation baculoviruses (P2), which were then used to induce expression of full-length basigin by addition at 1% v/v to Sf9 cells at roughly 2.5–3.0 million cells per ml. After 48 h, cells were harvested then resuspended in lysis buffer (25 mM Tris pH 8.0, 150 mM NaCl, 10% glycerol) supplemented with cOmplete EDTA-free protease inhibitors (Roche). Cells were lysed using a Dounce homogenizer followed by sonication on ice (60% amplitude, 3 s pulse, 9 s rest for 1.5 min). Lysed homogenate was clarified by centrifugation at 3,000*g* for 20 min, then the supernatant further spun at 100,000*g* for 45 min at 4 °C to isolate membranes. Following resuspension in lysis buffer, membranes were solubilized with 1.2% dodecyl-β-D-maltoside (DDM) for 1 h at 4 °C. Following centrifugation at 100,000*g* for 45 min at 4 °C, the supernatant with incubated with Ni-NTA resin (Qiagen) at 4 °C for 1 h and then the resin was washed (25 mM Tris pH 8.0, 300 mM NaCl, 10% glycerol, 0.02% DDM and 15 mM imidazole). Bound proteins were eluted using 25 mM Tris pH 8.0, 150 mM NaCl, 10% glycerol, 0.02% DDM and 400 mM imidazole then further purified on an S200 Increase 10/300 column into buffer containing 20 mM HEPES pH 7.2, 150 mM NaCl and 0.02% DDM:cholesteryl hemisuccinate (10:1 w/v ratio). Approximately 100–200 µg of full-length basigin was obtained from 100 ml of Sf9 cell culture.

Basigin ectodomain was expressed and purified as reported previously[3].

Structure determination using cryo-EM

To prepare a complex of PfRH5–PfCyRPA–PfRIPR–Cy.003 Fab for cryo-EM analysis, purified proteins were incubated together at an equimolar ratio in HBS for 5 min at room temperature. Approximately 250 µg of complex was prepared. Following incubation, the mixture was subject to gel filtration using an S200 Increase 10/300 GL column equilibrated in HBS. Fractions containing the complex were concentrated with a 100 K Amicon Ultra centrifugal unit at 6,000*g* and 4 °C.

Cryo-EM grids were prepared with an FEI Vitrobot Mark IV (Thermo Fisher) at 4 °C and 100% humidity; 3 µl of complex at 0.2 mg ml^{-1} was applied to Au-Flat 1.2/1.3 grids (Protochips) that had been glow-discharged at 15 mA for 60 s. Following incubation for 5 s, grids were blotted for 1–4 s then plunged into liquid ethane.

Grids were imaged using an FEI Titan Krios operating at 300 kV and equipped with a Gatan BioQuantum energy filter (20 eV) and K3 direct electron detector. Data collection was automated using fast acquisition mode in EPU (Thermo Fisher). Images were acquired at a nominal ×58,149 magnification corresponding to a calibrated pixel size of 0.832 Å per pixel (0.416 Å per super-resolution pixel), at a dose rate of 16.32 electrons Å^{-2} s^{-1} and total exposure time of 3 s with 40 frames. This resulted in a total dose of 48.97 electrons Å^{-2}. Images were acquired using a 100 µm objective aperture with defocus range of −1.0 to −3.0 µm in 0.25 µm increments. Data were collected from three grids in back-to-back sessions, all prepared with the same sample. A total of 13,524 movies were acquired (7,428 from grid 1, 2,720 from grid 2 and 3,376 from grid 3).

Image processing

Movies were motion corrected and contrast transfer function parameters estimated on-the-fly in SIMPLE 3.0 (ref. 36). Datasets from each session were preprocessed individually. Micrographs were first template picked using templates from a previous pilot data collection and picked particles (1,202,046 from grid 1, 1,601,557 from grid 2 and 752,273 from grid 3, yielding a total of 2,555,876 particles) were extracted (box size of 416 pixels) and subject to two-dimensional classification separately. Following exclusion of particles from poorly defined two-dimensional classes, particles from all three sessions were exported to cryoSPARC v.3.3.2. Here, particles were subject to further rounds of two-dimensional classification and particle clean-up, yielding a combined total of 961,077 particles. These were used for ab initio reconstruction into six classes, which showed that the dataset contained three major species: the PfRCR–Cy.003 complex, a complex lacking PfRH5 (PfCyRPA–PfRIPR–Cy.003) and a complex of mostly PfCyRPA and Cy.003 alone.

Before further refinement, micrographs were repicked using the cryoSPARC implementation of TOPAZ[37], yielding a total of 2,615,684 particles. These were subject to rounds of two-dimensional classification to remove bad particles then combined with the previous SIMPLE-picked particles. Following removal of duplicates, a final particle stack of 1,686,994 unique particles was obtained. These particles were subject to heterogeneous refinement using volumes for complexes PfRCR–Cy.003, PfCyRPA–PfRIPR–Cy.003 and PfCyRPA–Cy.003, plus three decoy volumes. This separated the particles into PfRCR–Cy.003 (523,352 particles), PfCyRPA–PfRIPR–Cy.003 (527,499 particles), PfCyRPA–Cy.003 (413,374 particles), decoy 1 (107,015 particles), decoy 2 (97,538 particles) and decoy 3 (18,216 particles). Further homogeneous, then non-uniform refinement of PfRCR–Cy.003 and PfCyRPA–PfRIPR–Cy.003 particles yielded maps of 3.2 Å for PfRCR–Cy.003 and 3.3 Å for PfCyRPA–PfRIPR–Cy.003. Following Bayesian polishing of particles in RELION 3.1.3 using default settings[38] and local per-particle contrast transfer function refinement in cryoSPARC, a final non-uniform refinement yielded consensus maps of 3.0 Å for PfRCR–Cy.003 (500,277 particles) and 3.1 Å for PfCyRPA–PfRIPR–Cy.003 (506,797 particles). Anisotropy analysis of these consensus maps using three-dimensional FSC[39] and Fourier shell occupancy[40] analyses showed that the consensus PfRCR–Cy.003 map had a sphericity of 0.91 (ref. 39) with an anisotropy transition zone[40] of 2.7–3.5 Å, and the PfCyRPA–PfRIPR–Cy.003 map had a sphericity of 0.89 (ref. 39) with an anisotropy transition zone[40] of 2.7–3.8 Å.

In both maps the region corresponding to PfCyRPA and Cy.003 was better resolved than the rest of the complex, and PfRIPR was more poorly resolved. Therefore, particles for PfRCR–Cy.003 and PfCyRPA–PfRIPR–Cy.003 were downsampled twofold and individually subjected to three-dimensional variability analysis in cryoSPARC[24] with three orthogonal principal modes. The motion of each complex was visualized in Chimera[41] by exporting the output of two-dimensional variability analysis as a volume series containing 20 frames. This indicated that both complexes showed some continuous conformational heterogeneity, manifesting as a pivoting of PfRH5 and PfRIPR. This was largest in the third principal mode analysed for PfRCR–Cy.003 which showed that a portion of PfRIPR had become unresolved over the volume series whereas the portion in contact with PfCyRPA remained mostly unchanged.

The density for PfRH5 and PfRIPR in PfRCR–Cy.003 was improved by local refinement. PfRH5 was locally refined using a soft mask around PfRH5–PfCyRPA. Before local refinement of PfRIPR, a more homogeneous subset of particles was obtained using heterogeneous refinement and volume outputs from three-dimensional variability analysis. This subset (253,444 particles) was signal subtracted such that it contained signal for PfRIPR only and was then subject to local refinement, first using a soft mask around PfRIPR then around a subportion of PfRIPR, guided by the motions observed in three-dimensional variability analysis. This yielded a map for PfRIPR with a reported global resolution of 3.3 Å, sphericity[39] of 0.76 and anisotropy transition zone[40] of 2.8–3.9 Å. The same procedure was used for PfRIPR in PfCyRPA–PfRIPR–Cy.003 except that the full particle stack (506,797 particles) was used.

Some two-dimensional classes indicated that there was additional density for PfRIPR that was not resolved in these maps. To visualize this extra region, a subset of particles (62,817) was processed by non-uniform refinement using the PfRCR–Cy.003 volume low-pass filtered to 30 Å as a reference. This yielded a map showing a small region of additional density projecting from the middle of the PfRIPR core, with a reported global resolution of 4.0 Å. Refinement with wider masks around this region did not result in more of PfRIPR being resolved.

The local resolution of unsharpened maps was estimated using cryoSPARC. Composite maps for PfRCR–Cy.003 and PfCyRPA–PfRIPR–Cy.003 were generated from consensus and local refinement maps in PHENIX[42]. Maps were postprocessed using the default parameters of DeepEMhancer[43] to aid model building. All maps were rendered in ChimeraX[44].

Model building and refinement

To aid model building of the PfRCR–Cy.003 complex, the crystal structures of PfRH5 (PDB ID: 4U0Q, chain C)[3], the PfCyRPA–Cy.003 Fab complex (PDB ID: 7PI2, chains D–F)[5] and an AlphaFold2 (ref. 28) (v.2.1.1)-predicted model of PfRIPR (20–716, except residues 484–548) were docked into the PfRCR–Cy.003 composite map as starting models using ChimeraX. These were manually rebuilt with COOT and ISOLDE[45] in iterative cycles. The C-terminal tail of PfRH5 was built de novo. Regions of PfRIPR (the N terminus, from domain N2 to the end of EGF2, and EGFs 3 and 4) were lower resolution and less interpretable than the remainder of the composite map. The AlphaFold2 prediction of PfRIPR was used to guide building in these areas to place structural elements. To build the PfCyRPA–PfRIPR–Cy.003 complex, the crystal structure of the PfCyRPA–Cy.003 Fab complex (PDB ID: 7PI2, chains D–F)[5] and PfRIPR from the PfRCR–Cy.003 structure were rigid-body fitted into the PfCyRPA–PfRIPR–Cy.003 composite map as starting models then manually rebuilt using COOT. The region corresponding to PfRIPR in the PfCyRPA–PfRIPR–Cy.003 map was less well resolved than in the PfRCR–Cy.003 counterpart, especially around the periphery of PfRIPR. For this reason, following docking, the PfRIPR model from PfRCR–Cy.003 was largely unedited with no changes made to some regions (for example, the N terminus and around residues 661–667). In each case, models were refined in PHENIX using global minimization and secondary structure restraints against their respective composite maps (which had not been postprocessed).

The model of PfRCR–Cy.003 comprises PfRIPR residues 34–716 (except 124–137 and 479–557), PfCyRPA residues 33–358, PfRH5 residues 159–516 (except 242–303), Cy.003 light-chain residues 23–229 and Cy.003 heavy-chain residues 21–245 (except 156–166). The model of PfCyRPA–PfRIPR–Cy.003 comprises PfRIPR residues 34–716 (except 124–137 and 479–558), PfCyRPA residues 34–358 (except 69–73, 124–127, 245–249 and 319–323), Cy.003 light-chain residues 23–229 and Cy.003 heavy-chain residues 21–245 (except 156–166).

To aid with map interpretation in which density was not continuous for PfRIPR beyond Pro716, an AlphaFold2 model of PfRIPR truncated after EGF5 (residues 20–769) was generated. Docking this prediction into the PfRCR–Cy.003 map suggested that the remaining density probably corresponded to EGF5. In addition, a model of the tail of PfRIPR (residues 717–1,086, comprising EGF5 to its C terminus) was separately predicted. This was manually docked into the second 4.0 Å PfRCR–Cy.003 map, showing additional density for the tail of PfRIPR, to generate a composite model of full-length PfRIPR.

To identify structural homologues of PfRIPR domains, the built structure of the PfRIPR core (residues 34–716) and the AlphaFold2-predicted structure of the PfRIPR tail (residues 717–1,086) were analysed by DALI[46], searching against the PDB25 database.

XL-MS of the PfRCR complex

Chemical crosslinking was performed on two separate 100 pmol aliquots (100 μl at 0.2 mg ml^{-1}) of PfRCR in 100 mM phosphate buffer pH 7.4; 2 μl of 5 mM DSSO (Thermo Fisher) in 10% DMSO and 100 mM phosphate buffer pH 7.0 was then added for 1 h at room temperature and quenched with 8 μl of 5% (v/v) of hydroxylamine in water (Sigma-Aldrich). Next, 1 μl of 200 mM TCEP was added for 1 h at 55 °C and free thiol groups were alkylated with 1 μl of 380 mM Iodoacetamide (Thermo Fisher) for 30 min at room temperature in the dark. Sequential double digestions were performed with Sequencing Grade Modified Trypsin (Promega) and Sequencing Grade Chymotrypsin (Roche) at an enzyme:substrate weight ratio of 1:25 for 3 h, and then overnight at 37 °C in 100 mM phosphate buffer pH 7.4. Digests were diluted 1:4 with water containing 5 vol% DMSO and 0.1 vol% formic acid before nanoscale liquid chromatography–mass spectrometry (LC–MS) analysis.

Digested protein samples were subjected to nanoscale LC–MS analysis[47] using a Reprosil-Pur C18-AQ trapping column (20 mm length × 100 μm internal diameter, 5 μm particle size, 200 Å pore size) and a Reprosil-Pur C18-AQ analytical column (30 cm length × 50 μm internal diameter, 3 μm particle size, 125 Å pore size), both packed in-house. A 10 μl sample was loaded onto the trapping column at 3 μl min^{-1} of solvent A (0.1 vol% formic acid in water) for 10 min. The trapping column was then switched in line with the analytical column and gradients applied from 8 to 43% of solvent B (acetonitrile + 0.1 vol% formic acid) at 125 nl min^{-1}. The column effluent was subjected to electrospray ionization at a spray tip voltage of 2.1 kV and heated capillary temperature of 200 °C.

Mass spectra were acquired in an Orbitrap Fusion Lumos mass spectrometer (Thermo Fisher Scientific) operated in data-dependent acquisition mode. Full mass spectrometry scans were acquired with an Orbitrap readout (m/z scan range 350–1,500 Th, mass resolution 120,000 full-width at half-maximum and normalized automatic gain control (AGC) target of 100%). Collision-induced dissociation (CID) fragmentation spectra (employing 30% CID energy) from multiply charged (2+ to 8+) precursor ions were acquired with an Orbitrap readout at 15,000 full-width at half-maximum mass resolution, with ion injection time limited to 600 ms and a normalized AGC target of 100%. MS3 scans, acquired to identify the peptide partners of DSSO-cross-linked dipeptides, were triggered only following recognition of a 31.9721 Da (±10 ppm) mass difference for a mass spectral doublet in the MS2 scan having a partner intensity range of 10–100% (ref. 48). Both doublet partners were subjected to CID fragmentation (employing 35% CID energy) at a maximum injection time of 600 ms, normalized AGC target of 200% and ion trap readout for the MS3 scan.

Proteome Discoverer 2.5 (Thermo Fisher Scientific) containing the XlinkX search node was used to process LC–MS data and identify crosslinked peptides. Dynamic modifications (oxidation of methionine and deamidation of asparagine) and static carbamidomethyl modification of cysteine residues were included in the search. The XlinkX search node was used, with DSSO defined as a mass spectrometry-cleavable crosslinker on lysine, serine, threonine and tyrosine residues[49]. In addition, dead-end dynamic modifications on these residues as hydrolysed or amidated DSSO were included. Mass tolerances for MS1, MS2 and MS3 scans were set to 10 ppm, 50 ppm and 0.5 Da, respectively. The false discovery rate threshold for the XlinkX Validator was set to 1%. Identified crosslinks were visualized with xiNET[50] to validate and aid building of the PfRCR–Cy.003 cryo-EM structure using a Cα–Cα distance threshold of 35 Å (ref. 51), mapped and measured using ChimeraX.

Microscale thermophoresis

Full-length basigin and BSG$^{\text{ecto}}$ were fluorescently labelled with Alexa Fluor 488 using an Alexa Fluor 488 protein-labelling kit (Thermo Fisher) as recommended. Excess dye was removed by gel filtration on an S75 Increase 10/300 column using a buffer containing 20 mM HEPES pH 7.2 and 150 mM NaCl for BSG$^{\text{ecto}}$, or with the same buffer also containing 0.02% DDM:cholesteryl hemisuccinate (10:1 w/v ratio) for full-length basigin. To measure the binding of PfRH5 and PfRCR to BSG$^{\text{ecto}}$, a twofold dilution series of PfRH5 or PfRCR (concentration range 8 μM to 3.91 nM) was prepared in 20 mM Tris pH 8.0, 200 mM NaCl, 1 mg ml^{-1} salmon sperm DNA and 0.01% Tween-20. Basigin ectodomain was held at constant 0.25 μM throughout the dilution series. To measure the binding of PfRH5 and PfRCR to full-length basigin, a similar twofold dilution series of PfRH5 and PfRCR (concentration range 2 μM to 0.12 nM) was prepared in 20 mM Tris pH 8.0, 200 mM NaCl, 1 mg ml^{-1} salmon sperm DNA and 0.02% DDM. Full-length basigin was held at a constant concentration of 0.1 μM. The sample was incubated for 10 min and centrifuged at 10,000*g* for 10 min, then the supernatant was transferred to Monolith NT.114 series premium capillaries (NanoTemper). Experiments were performed at 25 °C on a Monolith NT.115. Because significant variations in raw fluorescence were observed for both PfRH5 and PfRCR measurements against full-length basigin (at over 2 μM) and basigin ectodomain (at over 5 μM) during data collection, data from these concentrations were excluded from analysis. Binding experiments were performed in triplicate for two separately prepared samples. Data were analysed using software v.1.5.41 (NanoTemper).

Surface plasmon resonance

PfRIPR and PfRIPR tail were immobilized onto separate flow paths of a CM5 Series S Sensor Chip (Cytiva) using the standard amine-coupling protocol, yielding approximately 8,000 response units for PfRIPR and around 2,000 for PfRIPR tail. The PfCSS–PfPTRAMP heterodimer complex was prepared at either 8.0 or 7.7 μM in SPR buffer (20 mM HEPES pH 7.5, 150 mM NaCl, 0.01% Tween-20), then a twofold serial dilution series was prepared in the same buffer. SPR traces were recorded on a T200 Biacore instrument (Cytiva) in SPR buffer at 25 °C, at a flow rate of 30 μl min^{-1} and either 150 or 180 s injections. Experiments were performed four times with four independent dilution series, and binding affinities estimated by steady-state analysis using T200 Biacore Evaluation Software (Cytiva).

Design and expression of cysteine-locked PfRH5

The Rosetta Disulfidize[52] protocol was used to design cysteine locks in PfRH5. Both wild-type and thermally stabilized PfRH5 crystal structures (PBD ID: 6RCO[4] and 5MI0 (ref. 53)) were used for design simulations. Following the introduction of cysteine locks, the designed models were relaxed using the Rosetta FastRelax[54] protocol. The top-scoring models based on both 'total_score' and 'dslf_fa13'[55] were manually inspected, and five disulfide cysteine-lock designs connecting the N- and C-terminal halves of PfRH5 were selected for experimental validation. The Rosetta Disulfidize and Rosetta FastRelax scripts used for model design are provided in Source Data. The selected disulfide locks (CC1, CC2, CC3, CC4 or CC5) were introduced into PfRH5ΔNL (a recombinant construct of PfRH5 lacking its N terminus and the α2–α3 internal loop, with the substitution C203Y (of the 7G8 *P. falciparum* strain))[3], then wild-type PfRH5ΔNL and the cysteine-locked designs were expressed from stable S2 cell lines, as described above for full-length PfRH5. Culture supernatants were harvested after 3–4 days, 0.45 μm filtered and incubated with CaptureSelect C-tagXL resin (Thermo Scientific). Beads were washed using ten column volumes of either PBS or TBS (25 mM Tris pH 7.5, 150 mM NaCl) and bound proteins eluted with five column volumes of C-tag elution buffer (25 mM Tris pH 7.4, 2 M $MgCl_2$). Eluted proteins were further purified by size exclusion chromatography using an S75 Increase 10/300 column with a running buffer of PBS or TBS (25 mM Tris pH 7.5, 150 mM NaCl). Following biophysical characterization of cysteine-lock designs CC1–CC5, a final cysteine-locked version of PfRH5 (PfRH5$^{\text{CL}}$) was generated through combination of cysteine locks CC1 and CC5. These were introduced into PfRH5ΔNL, then expressed and purified as for other single-cysteine-lock versions.

Circular dichroism of cysteine-locked PfRH5

Circular dichroism spectra of wild-type PfRH5ΔNL and single-cysteine-lock designs (CC1–CC5) were recorded at 50 μg ml^{-1} in PBS buffer at 200–250 nm wavelength with a temperature ramp increasing by increments of 2 °C from 20 to 90 °C. PfRH5ΔNL and double-cysteine-locked PfRH5ΔNL^{CL} were buffer exchanged into 10 mM sodium phosphate pH 7.5 and 50 mM NaF with Zeba Spin Desalting Columns, followed by circular dichroism spectra recorded at 75 μg ml^{-1} and 190–250 nm with temperature ramp increasing by increments of 2 °C from 20 to 90 °C. A Jasco J-815 Spectropolarimeter was used for all measurements. Data analysis was performed using GraphPad Prism v.8.4.3.

Maleimide-PEG2-biotin labelling of cysteine-locked PfRH5

PfRH5ΔNL^{CL} (10 μg) was buffer exchanged into denaturing buffer (6 M guanidine hydrochloride, 100 mM sodium acetate pH 5.5) using a 0.5 ml 7 K MWCO Zeba Spin Desalting Column (Thermo Scientific, catalogue no. 89882) with incubation at 37 °C for 30 min. EZ-Link maleimide-PEG2-biotin stock (Thermo Scientific, catalogue no. 21901BID) was prepared at 15 mg ml^{-1} in DMSO and diluted to 3 mg ml^{-1} with 100 mM sodium acetate pH 5.5 immediately before use. Denatured PfRH5ΔNL^{CL} was labelled with a 150× molar excess of maleimide-PEG2-biotin at room temperature for 1 h. Excess maleimide-PEG2-biotin was removed by performing buffer exchange into the denaturing buffer using a 0.5 ml 7 K MWCO Zeba Spin Desalting Column. The above steps were carried out with and without the addition of 5 mM TCEP (Thermo Scientific, catalogue no. 77720) during the denaturation step. The extent of maleimide-PEG2-biotin labelling was then assessed by intact mass analysis using mass spectrometry.

Intact mass analysis of maleimide-labelled, cysteine-locked PfRH5

Reversed-phase chromatography was performed in-line before mass spectrometry using an Agilent 1100 high-performance liquid chromatography system (Agilent Technologies). Concentrated protein samples were diluted to 0.02 mg ml^{-1} in 0.1% formic acid, and 50 μl was injected onto a 2.1 × 12.5 mm^2 Zorbax 5 μm 300SB-C3 guard column housed in a column oven set at 40 °C. The solvent system used consisted of 0.1% formic acid in ultrahigh-purity water (Millipore) (solvent A) and 0.1% formic acid in methanol (LC–MS grade, Chromasolve) (solvent B). Chromatography was performed as follows: initial conditions were 90% A and 10% B and a flow rate of 1.0 ml min^{-1}. After 15 s at 10% B, a two-stage linear gradient from 10% to 80% B was applied over 45 s and then from 80 to 95% B over 3 s. Elution then proceeded isocratically at 95% B for 72 s followed by equilibration at initial conditions for a further 45 s. Protein intact mass was determined using a 1969 MSD-ToF electrospray ionization orthogonal time-of-flight mass spectrometer (Agilent Technologies). The instrument was configured with the standard electrospray ionization source and operated in positive-ion mode. The ion source was operated with capillary voltage 4,000 V, nebulizer pressure 60 pounds per square inch gauge, drying gas 350 °C and drying gas flow rate 12 l min^{-1}. The instrument ion optic voltages were as follows: fragmentor 250 V, skimmer 60 V and octopole RF 250 V.

Modelling of PfPCRCR–antibody complexes

For visualization of PfRCR in the context of the erythrocyte surface, structure-based alignments were used to dock PfRCR onto membrane-bound basigin using crystal and cryo-EM-derived structures, either determined in this study or previously published. To achieve this, the model of PfRIPR (derived from the PfRIPR core determined here by cryo-EM and AlphaFold2 prediction of the PfRIPR tail, docked onto one another as detailed above) was first aligned onto the PfRCR–Cy.003 complex cryo-EM structure to generate a full-length model of PfRCR. Next, the crystal structure of PfRH5 bound to BSG^{ecto} (PDB ID: 4U0Q)[3] was aligned onto the PfRH5 component of PfRCR. This basigin–PfRCR–Cy.003 composite model was then aligned onto either MCT1-bound basigin (PDB ID: 7CKR)[33] or PMCA-bound basigin (PDB ID: 6A69)[34] using the D2 domain of basigin as a target. To assess the location of neutralizing PfCyRPA epitopes in this erythrocyte-bound context of the PfRCR complex, crystal structures of PfCyRPA-bound Cy.004 (PDB ID: 7PHW)[5], Cy.007 (PDB ID: 7PHV)[5], 8A7 (PDB ID: 5TIH)[19] and c12 (PDB ID: 5EZO)[20] were aligned onto the PfRCR complex using PfCyRPA as a target. Structural alignments were performed in COOT or ChimeraX.

Flow cytometry analysis of PfRCR binding to erythrocytes

Erythrocytes (O$^+$ or O$^-$) were washed twice in PBS containing 1% w/v bovine serum albumin (PBS/BSA), then 50 μl aliquots containing approximately 10 million cells were prepared. PfRCR was prepared by mixing equimolar amounts of PfRH5ΔN[3], PfCyRPA and PfRIPR in PBS/BSA followed by incubation at room temperature for 30 min. Where the blocking activity of anti-PfRH5 or anti-PfCyRPA monoclonal antibodies was being assayed, these were included at twofold molar excess during this incubation period. Following this, aliquots of erythrocytes were centrifuged at 1,000*g* for 1 min, the supernatant removed and cells resuspended with the prepared protein complexes and incubated for 1 h at room temperature on a roller. Following this incubation period, red blood cells were recovered by spinning as before then washed twice in PBS/BSA. To quantify the binding of PfRCR to erythrocytes, samples were stained in one of two ways as detailed below, then washed three times with PBS/BSA followed by dilution to approximately 6 million cells per ml before analysis with a S3e Cell Sorter operated with ProSort Software v.1.6.0.12 (Bio-Rad). For each sample, binding was performed in a volume of 50 μl and 50,000 events were recorded. Data were analysed using FlowJo v.10.9 (Becton Dickinson). Erythrocytes were gated by plotting forward-scatter area against side-scatter area, then singlets were identified by plotting forward-scatter area against forward-scatter height. Positively labelled erythrocytes corresponding to those with bound PfRCR were identified by plotting forward-scatter area against Alexa Fluor 488 area, with positive-gate placement guided by unstained red blood cells and those incubated with detection antibodies/nanobodies only (Supplementary Fig. 2). The number of positive cells is expressed as a percentage of the number of singlets recorded. Statistical analyses were performed using GraphPad Prism v.9.2.0.

To verify that the non-neutralizing anti-PfRH5 antibody R5.011 (ref. 4) could be used to quantify PfRCR binding to erythrocytes without reducing PfRCR binding, we first studied PfRCR that had been labelled using the CaptureSelect Alexa Fluor 488 Anti-C-tag Conjugate (no. 7213252100, Thermo Scientific). Following incubation of erythrocytes with 2 μM PfRCR, alone or in the presence of 4 μM anti-PfRH5 antibodies R5.004 or R5.011 (ref. 4), cells were washed and incubated with CaptureSelect Alexa Fluor 488 Anti-C-tag Conjugate for 1 h at room temperature in the dark. Erythrocyte binding was then quantified as above, measured in duplicate.

To assay the ability of anti-PfCyRPA antibodies to block PfRCR binding to erythrocytes, these were incubated with either 400 nM PfRCR alone or in the presence of 800 nM anti-PfCyRPA antibodies Cy.003, Cy.004 or Cy.007 (ref. 5). The anti-PfRH5 antibody R5.004, which blocks PfRH5 binding to basigin[4], was used as a positive control. Following incubation with protein complexes, erythrocytes were washed and stained by incubation with the monoclonal anti-PfRH5 antibody R5.011 as a primary antibody, followed by washing once then incubation with goat anti-human IgG cross-adsorbed Alexa Fluor 488 secondary antibody (no. A11013, Invitrogen). Primary and secondary antibodies were each used at 10 μg ml^{-1} in PBS/BSA for 1 h at room temperature in the dark. Erythrocyte binding was then quantified as above, measured in triplicate. Because Cy.004 binds to PfCyRPA in a calcium-dependent manner[5], cells were supplemented with 1 mM $CaCl_2$

during protein incubation with this antibody. As a control, PfRCR alone was incubated with red blood cells both in the presence and absence of 1 mM $CaCl_2$, with no significant change in the number of positive cells observed.

Haemolysis assay

Red blood cells (100 µl) were washed twice by dilution in 10 ml of PBS followed by spinning at 500*g* for 5 min, then diluted to approximately 4 million cells per ml in PBS. Next, 200 µl of diluted cells was aliquoted into wells of a 96-well plate then spun once more at 500*g* for 5 min and the supernatant discarded. Cells were then resuspended in either 200 µl of PBS containing 2 µM PfRH5, 2 µM PfCyRPA, 2 µM PfRIPR and 2 µM PfRCR or 2 µM alpha-haemolysin (Sigma) for 24 h at 37 °C. In addition, PBS containing 1% v/v Triton X-100 or PBS alone was used as positive and negative control, respectively. Following incubation, cells were spun at 500*g* for 5 min then 50 µl of each solution transferred to a new 96-well plate. Absorbance at 405 nm was used to assess the degree of haemolysis using a microplate reader (Tecan). For each protein sample group, background signal observed with PBS alone was subtracted then haemolysis reported relative to complete cell lysis, as in the positive control (1% Triton X-100). Data were collected four times independently for all samples except for PfRIPR, which was collected in duplicate. Statistical analyses were performed using GraphPad Prism v.9.2.0.

Calcium flux assay

Erythrocytes (O^+) were loaded with Fluo-4 through their incubation with 6 µM Fluo-4AM in RPMI (supplemented with 0.5% w/v AlbuMAX (Gibco) and 4 g l^{-1} glucose) for 1 h at 37 °C. Following washing and resting of these Fluo-4-loaded erythrocytes for 15 min, recombinant protein (PfRH5, PfRH5ΔN or PfRCR) was added to the cells at 2 µM in RPMI then fluorescence (excitation 488 nm, emission 535 nm) was measured over 800 s in black-bottomed, 384-well plates in a CLARIOstar microplate reader with software v.5.6.0 R2 (BMG Labtech). RPMI alone was used as a negative control. Measurements were recorded in technical triplicate. To verify the loading of Fluo-4 into erythrocytes, lysis was induced by the addition of 0.1% v/v Triton X-100 in RPMI and fluorescence measured as above. Untreated erythrocytes were used as a control.

P. falciparum culture and transfection

Blood-stage *P. falciparum* parasites were cultured in human erythrocytes (UK NHS Blood and Transplant) at 3% haematocrit with custom RPMI-1640 medium supplemented with 2 mM L-glutamine, according to previously established methods[56]. All parasites used in this study were derived from *P. falciparum* line *p230p*DiCre, generated in strain 3D7 (ref. 44). Parasites were synchronized by purification of schizont stages using a Percoll gradient, facilitating reinvasion, followed by sorbitol treatment of newly formed ring stages.

Transfections were performed as previously described[57]. Transgenic parasites were further cloned by limiting dilution. For induction of dimerizable, Cre-mediated excision of floxed DNA, early-ring-stage parasites were treated with 10 nM rapamycin or DMSO as control. Parasite samples for PCR and immunoblot analysis were collected around 40–42 h following rapamycin treatment.

Generation and genotyping of transgenic *P. falciparum* parasites

CRISPR–Cas9 guide RNA sequences targeting either the 5' region (guide 1: 5'GCTATATAAACATATTTACG-3' and guide 2: 5'-TTTGAAT TTACTATATGTAC-3') or the 3' region of the *PfRh5* open reading frame (5'-TTGTCATTTCATTGTGTAAG-3') were identified using EuPaGDT (http://grna.ctegd.uga.edu/). Each guide was cloned into vector pDC2-Cas9-hDHFRyFCU[57], generating plasmids pDC2-Cas9-5'guide1, pDC2-Cas9-5'guide2 and pDC2-Cas9-3'guide. All primers used to generate DNA repair plasmids, along with templates and expected PCR product sizes, are listed in Supplementary Tables 1 and 2.

A DNA repair template designed to replace the endogenous *PfRh5* intron with a synthetic *SERA2 LoxP* intron (*LoxPint*)[27] was synthesized with 300–350-base-pair homology regions spanning the *PfRh5* 5′ untranslated region (UTR) and coding regions on either side of the endogenous intron. Homology region 1 (amplified with primers 1 and 2) started at 5'-GGTAAATGTAGGATTGTTCT-3' and ended at 5'-ATAATGGTCAAAATTAATTT-3', and homology region 2 (amplified with primers 3 and 4) spanned 5'-GATTAAGTTTTGAAAATGCA-3' to 5'-ATCCACATTTTTATAGTCTT-3'. Both homology arms, and the intervening *SERA2 LoxPint* module (amplified with primers 5/6), were stitched together using overlapping extension PCR (using primers 1 and 6, followed by primers 1 and 4). The final PCR product was inserted into pGEM-T Easy (Promega), linearized using NcoI/SpeI and mixed with plasmid pDC2-Cas9-5' guide1 and pDC2-Cas9-5' guide2 before transfection, generating line $PfRH5^{NT}$.

A DNA repair template for insertion of a *LoxP* sequence plus half of the *SERA2* intron (5'-ATAACTTCGTATAGCATACATTATA CGAAGTTATTATATATGTATATATATATATATTTATATATTTTATATTCTTT TAG (*LoxP* sequence underlined)) directly after the *PfRh5* stop codon was synthesized with a 300–350-base-pair homology region spanning the coding and 3' UTR regions on either side of the *PfRh5* C-term Cas9 cut site. Homology region 1 (amplified with primers 10 and 11) started at 5'-GAATTGAATATCATACAAAA and ended at 5'-GTAAGTGGTTTATTTTTTTT. Homology region 2 (amplified with primers 12 and 13) started at 5'-AATGACAAAACATGGTATGT and ended at 5'-CAAGTACGAGCATCCGGAAC. Part of the *LoxPint* module was amplified with primers 14 and 6. All three PCR products were subsequently fused using overlapping extension PCR with primers 10 and 6 followed by 10 and 13. The final PCR product was inserted into pGEM-T Easy (Promega), generating plasmid p*PfRh5*_C-term_*LoxP*. Finally this plasmid was linearized with EcoRI, mixed with pDC2-Cas9-3'guide and transfected into line $PfRH5^{NT}$, generating line $PfRH5^{cKO}$.

For generation of a parasite line containing an inducible mutant *PfRh5* gene, a second copy of *PfRh5* was designed for integration 3' to the floxed, endogenous *PfRh5* copy. Following rapamycin-induced excision of the floxed endogenous locus, the downstream *Rh5* copy would be expressed. For this, a recodonized *PfRh5* sequence was synthesized (GeneArt) starting 3' to the endogenous intron. This recodonized sequence was then flanked by a 5' homologue region (spanning the last 546 base pairs of the endogenous PfRh5 sequence and half of the *LoxPint* module described above) and a 3' homologue region spanning 595 base pairs of the *PfRh5* 3' UTR. The 5' homologue region was synthesized by overlapping extension PCR (using primers 21 and 22, 10 and 23, followed by 21 and 23) and inserted into the GeneArt-generated plasmid using SacII/AflII (homologue region 1 started at 5'-CTTTCATGTTACAATAATAA and ended at 5'-GTAAGTGGTTTATTTTTTTT). The 3' homologue region was also assembled by overlapping extension PCR (using primers 13, 18, 19 and 20 followed by 18 and 20), starting at 5'-AATGACAAAACATGGTATGT and ending at 5'-TGATATAAATGAAGCGTTGA. The final PCR product was inserted into the plasmid via MfeI/SalI, generating the final plasmid, p*PfRh5*_WT_sec_copy. Finally the plasmid was digested using NcoI/NotI, mixed with pDC2-Cas9-3'guide and transfected into the transgenic $PfRH5^{NT}$ parasite line, generating line $PfRH5^{WT}$.

For generation of a parasite line expressing a locking-cysteines *PfRh5* mutant on rapamycin-induced excision of the endogenous floxed *PfRh5 gene*, plasmid p*PfRh5*_WT_sec_copy was modified to introduce the following mutations: L164C, E239C, M478C and H489C. Mutations L164C and E239C were introduced with primers via overlapping extension PCR (using primers 25 and 26, 27 and 28, followed by 25 and 29) using p*PfRh5*_WT_sec_copy as template. The final PCR product was cloned into plasmid p*PfRh5*_WT_sec_copy using AflII/NdeI, yielding plasmid p*PfRh5*_lockingCyst_sec_copy_A. Likewise, mutations M478C and H489C were also introduced by PCR amplification (using primers 30 and 31, 32 and 33, then 30 and 33), followed by cloning of this

DNA fragment into plasmid p*PfRh5*_lockingCyst_sec_copy_A using BamHI/MfeI restriction enzymes, yielding plasmid p*PfRh5*_lockingCyst_sec_copy_B. This plasmid was digested using NcoI/NotI, mixed with pDC2-Cas9-3'guide and transfected into the transgenic PfRH5$^{\text{NT}}$ parasite line, generating line PfRH5$^{\text{CL}}$.

All plasmid DNA sequences were verified by Sanger sequencing. Positions of diagnostic primers used to genotype transgenic parasites are shown in schematics in Extended Data Fig. 6a,b. Diagnostic primer sequences along with expected PCR product sizes are listed in Supplementary Tables 1 and 2. A positive-control PCR reaction using primers 36 and 37 to amplify a 737-base-pair product from the *PfRON2* locus was also included in each set of diagnostic PCRs.

The Qiagen DNeasy Blood and Tissue kit was used for all genomic DNA extractions. All diagnostic PCR analyses were performed using GoTaq Green (Promega) under the following conditions: 5 min at 95 °C, 33 cycles of 30 s at 95 °C, 30 s at 55 °C then 1 min at 30 s kb^{-1} and 64 °C. For amplification of fragments for construct synthesis, CloneAmp HiFi polymerase (Takara) was used. A typical reaction was run with 32 cycles of 5 s at 98 °C, 15 s at 55 °C and 10 s kb^{-1} at 68 °C.

Immunoblotting

Synchronized schizonts were harvested by Percoll gradient centrifugation, washed in RPMI-1640 without AlbuMax and lysed in SDS sample buffer containing 100 mM dithiothreitol before protein separation on precast Bis-Tris polyacrylamide gels (MPAGE, Merck) and transfer to nitrocellulose membranes by electroblotting. Blots were blocked overnight in 5% milk in PBS with 0.2% Tween-20 and subsequently incubated with either rat anti-PfHSP70 (1:1,000)[58] or rabbit anti-PfRh5 (1:5,000)[59], followed by either goat anti-rat horseradish peroxidase (HRP, Sigma) or goat anti-rabbit HRP (Bio-Rad). Detection using enhanced chemiluminescence was carried out using Immobilon Western Chemiluminescent HRP Substrate (Millipore).

Parasite growth assay

To determine the growth rate of mutant parasites relative to wild-type parasites, ring-stage DMSO and rapamycin-treated cultures were adjusted to a parasitaemia of roughly 0.8% and 2% haematocrit and grown in a gassed chamber at 37 °C. A starting parasitaemia was taken when parasites reached the schizont stage of the same cycle (cycle 0), and again after a further 40 h or so with parasites at schizont stage in cycle 1. Parasitaemia was measured following fixation of cells with 4% paraformaldehyde and 0.1% glutaraldehyde (Sigma) in PBS for 1 h at room temperature, followed by incubation for 1 h at 37 °C with SYBR Green I (Life Technologies).

For flow cytometry analysis, a LSR Fortessa X-20 with BD FACSDiva Software v.9.0 was used with a 530/30 filter, counting 30,000 singlet events per sample. Gating for erythrocytes was achieved by plots of forward-scatter area against side-scatter area (gate P1). Doublet discrimination required gating of forward-scatter area against forward-scatter width (gate P2), followed by side-scatter area against side-scatter width (gate P3). A SYBR Green-stained, uninfected erythrocyte sample was used as a negative control. Gating of SYBR Green-infected erythrocytes was achieved by plotting side-scatter area against Alexa Fluor 488 area using the 530/30 standard filter (gate P4). Parasitaemia was determined by the number of cells identified in gate P4 as a percentage of those in gate P3 (Supplementary Fig. 3). Data were analysed using FlowJo v.10. GraphPad Prism v.9.0.0 was used for statistical analysis (two-tailed, unpaired *t*-test) and graph generation.

Live-cell imaging of calcium fluxes

For calcium flux assays, erythrocytes were first incubated with 5 µM Fluo-4AM (Invitrogen) in IMDM medium containing 2.5 mM CaCl_2 and 5 mM Na-pyruvate for 1 h. Cells were subsequently washed three times and then allowed to rest at 37 °C for 30 min. Purified schizonts were added to labelled erythrocytes in a 10–15% parasitaemia and 3% haematocrit culture before dilution to 0.3% haematocrit in the same medium. Cultures were loaded into poly-L-lysine-coated µ-Slide VI 0.4 (Ibidi) channel slides and transferred to a Nikon Ti E inverted-microscope chamber prewarmed to 37 °C. Samples were imaged using a ×60 oil-immersion objective and an ORCA Flash 4.0 CMOS camera (Hamamatsu), at a rate of one frame per second. Videos were acquired and processed using the NIS Advanced Research software package. A total of 41 invasion events were recorded for both PfRH5$^{\text{WT}}$ and PfRH5$^{\text{CL}}$ parasites, using parasites derived from three biological replicates. All statistical analysis was performed using Prism v.9.0.

Reporting summary

Further information on research design is available in the Nature Portfolio Reporting Summary linked to this article.

Data availability

Cryo-EM maps for PfRCR–Cy.003 are available from the Electron Microscopy Data Bank under accession codes EMDB-16569, EMDB-16637, EMDB-16638, EMDB-16639 and EMDB-16640, and its coordinates from the Protein Data Bank under accession code 8CDD. Cryo-EM maps for PfCyRPA–PfRIPR–Cy.003 are available under accession codes EMDB-16570, EMDB-16636 and EMDB-16635, and its coordinates from the Protein Data Bank under accession code 8CDE. In this study, previously published structures have been used for structural analysis; these can be found in the Protein Data Bank under accession codes 1IGT, 4HL0, 4U0Q, 4U0R, 4U1G, 5EZO, 5FTT, 5TIH, 5TIK, 6A69, 6RCU, 6RCV, 6Z2L, 7CKR, 7PHU, 7PHV, 7PHW, 7PI2 and 7UNY. Uncropped gels and source data for all graphs generated in this study are provided in Supplementary figures and Source data, respectively. The Rosetta Disulfidize and Rosetta FastRelax scripts used to design the cysteine-locked version of PfRH5 in this manuscript are also provided in Source data. All other data are available from the authors on request.

Code availability

Rosetta scripts used in this study and coordinates for composite molecular models are provided in Source data.

35. Hjerrild, K. A. et al. Production of full-length soluble *Plasmodium falciparum* RH5 protein vaccine using a *Drosophila melanogaster* Schneider 2 stable cell line system. *Sci. Rep.* **6**, 30357 (2016).
36. Caesar, J. et al. SIMPLE 3.0. Stream single-particle cryo-EM analysis in real time. *Biol. X* **4**, 100040 (2020).
37. Bepler, T. et al. Positive-unlabeled convolutional neural networks for particle picking in cryo-electron micrographs. *Nat. Methods* **16**, 1153–1160 (2019).
38. Zivanov, J., Nakane, T. & Scheres, S. H. W. A Bayesian approach to beam-induced motion correction in cryo-EM single-particle analysis. *IUCrJ* **6**, 5–17 (2019).
39. Tan, Y. Z. et al. Addressing preferred specimen orientation in single-particle cryo-EM through tilting. *Nat. Methods* **14**, 793–796 (2017).
40. Vilas, J. L. & Tagare, H. D. New measures of anisotropy of cryo-EM maps. *Nat. Methods* **20**, 1021–1024 (2023).
41. Pettersen, E. F. et al. UCSF Chimera—a visualization system for exploratory research and analysis. *J. Comput. Chem.* **25**, 1605–1612 (2004).
42. Liebschner, D. et al. Macromolecular structure determination using X-rays, neutrons and electrons: recent developments in Phenix. *Acta Crystallogr. D Struct. Biol.* **75**, 861–877 (2019).
43. Sanchez-Garcia, R. et al. DeepEMhancer: a deep learning solution for cryo-EM volume post-processing. *Commun. Biol.* **4**, 874 (2021).
44. Pettersen, E. F. et al. UCSF ChimeraX: structure visualization for researchers, educators, and developers. *Protein Sci.* **30**, 70–82 (2021).
45. Croll, T. I. ISOLDE: a physically realistic environment for model building into low-resolution electron-density maps. *Acta Crystallogr. D Struct. Biol.* **74**, 519–530 (2018).
46. Holm, L. Dali server: structural unification of protein families. *Nucleic Acids Res.* **50**, W210–W215 (2022).
47. Meiring, H. D., van der Heeft, E., ten Hove, G. J. & de Jong, A. P. J. M. Nanoscale LC–MS(n): technical design and applications to peptide and protein analysis. *J. Sep. Sci.* **25**, 557–568 (2002).
48. Kao, A. et al. Development of a novel cross-linking strategy for fast and accurate identification of cross-linked peptides of protein complexes. *Mol. Cell. Proteomics* **10**, M110.002212 (2011).

49. Iacobucci, C. et al. First community-wide, comparative cross-linking mass spectrometry study. *Anal. Chem.* **91**, 6953–6961 (2019).
50. Combe, C. W., Fischer, L. & Rappsilber, J. xiNET: cross-link network maps with residue resolution. *Mol. Cell. Proteomics* **14**, 1137–1147 (2015).
51. Keller, A., Chavez, J. D., Felt, K. C. & Bruce, J. E. Prediction of an upper limit for the fraction of interprotein cross-links in large-scale in vivo cross-linking studies. *J. Proteome Res.* **18**, 3077–3085 (2019).
52. Fenn, L. S., Kliman, M., Mahsut, A., Zhao, S. R. & McLean, J. A. Characterizing ion mobility-mass spectrometry conformation space for the analysis of complex biological samples. *Anal. Bioanal. Chem.* **394**, 235–244 (2009).
53. Campeotto, I. et al. One-step design of a stable variant of the malaria invasion protein RH5 for use as a vaccine immunogen. *Proc. Natl Acad. Sci. USA* **114**, 998–1002 (2017).
54. Nivon, L. G., Moretti, R. & Baker, D. A Pareto-optimal refinement method for protein design scaffolds. *PLoS ONE* **8**, e59004 (2013).
55. Alford, R. F. et al. The Rosetta all-atom energy function for macromolecular modeling and design. *J. Chem. Theory Comput.* **13**, 3031–3048 (2017).
56. Trager, W. & Jensen, J. B. Human malaria parasites in continuous culture. *Science* **193**, 673–675 (1976).
57. Knuepfer, E., Napiorkowska, M., van Ooij, C. & Holder, A. A. Generating conditional gene knockouts in *Plasmodium* – a toolkit to produce stable DiCre recombinase-expressing parasite lines using CRISPR/Cas9. *Sci. Rep.* **7**, 3881 (2017).
58. Schlott, A. C. et al. Inhibition of protein N-myristoylation blocks *Plasmodium falciparum* intraerythrocytic development, egress and invasion. *PLoS Biol.* **19**, e3001408 (2021).
59. Douglas, A. D. et al. The blood-stage malaria antigen PfRH5 is susceptible to vaccine-inducible cross-strain neutralizing antibody. *Nat. Commun.* **2**, 601 (2011).
60. The Plasmodium Genome Database Collaborative. PlasmoDB: an integrative database of the *Plasmodium falciparum* genome. Tools for accessing and analyzing finished and unfinished sequence data. *Nucleic Acids Res.* **29**, 66–69 (2001).

Acknowledgements This work was funded through a Wellcome Investigator award (no. 220797/Z/20/Z) to M.K.H. Crosslinking mass spectrometry analysis of the PfRCR complex was funded through H2020 TRANSVAC2 Grant Agreement no. 730964. Cy.003 was produced through the European Commission FP7 EURIPRED project (no. INFRA-2012-312661), funded by the European Union's Seventh Framework Programme (FP7/2007—2013) under Grant Agreement no. 312661—European Research Infrastructures for Poverty Related Diseases (EURIPRED). We thank R. Matadeen, J. Caesar and T. Matthews-Palmer at the COSMIC cryo-EM facility (University of Oxford) for support with data collection and data processing. We thank the Imaging and Cytometry Platform for Infection Biology at The London School of Hygiene & Tropical Medicine for the use of their Nikon Ti2 microscope, which was used to perform live-cell-invasion imaging work. We thank L. van der Maas and H. D. Meiring (Intravacc) and R. Chalk (University of Oxford) for support with mass spectrometry. We also thank the NHS Blood and Transplant services for the supply of human blood for parasite culture and flow cytometry assays; and for PlasmoDB[60], hosted by the VEuPathDB resource centre for providing *Plasmodium* genomic DNA sequences.

Author contributions B.F. expressed and purified proteins and performed structure determination, surface plasmon resonance analysis and FACS analysis. N.A. designed, produced and performed biophysical characterization of cysteine-locked PfRH5. M.N.H. and E.K. generated transgenic parasite lines and assessed the effect of cysteine-locked PfRH5 on invasion and calcium fluxes. A.J. produced full-length basigin and conducted basigin-binding studies. R.J.R. and S.J.D. contributed XL-MS and haemolysis data. H.W.-M, contributed protein reagents. E.K. and M.K.H. designed experiments and contributed expertise and funding. B.F. and M.K.H. prepared the manuscript and all authors contributed and commented on it.

Competing interests M.K.H. and S.J.D. are named inventors on patents related to the use of PfRH5 as a vaccine (no. GB2105/052205), to the design of a thermally stabilized version of PfRH5 for use as a vaccine (no. GB2017/052608) and to mAbs targeting PfRH5 (no. GB2019/052885). B.F., N.A., M.N.H., A.J., R.J.R., H.W.-M. and E.K. declare no competing interests.

Additional information

Supplementary information The online version contains supplementary material available at https://doi.org/10.1038/s41586-023-06856-1.

Correspondence and requests for materials should be addressed to Matthew K. Higgins.

Peer review information *Nature* thanks Louis Miller and the other, anonymous, reviewer(s) for their contribution to the peer review of this work. Peer reviewer reports are available.

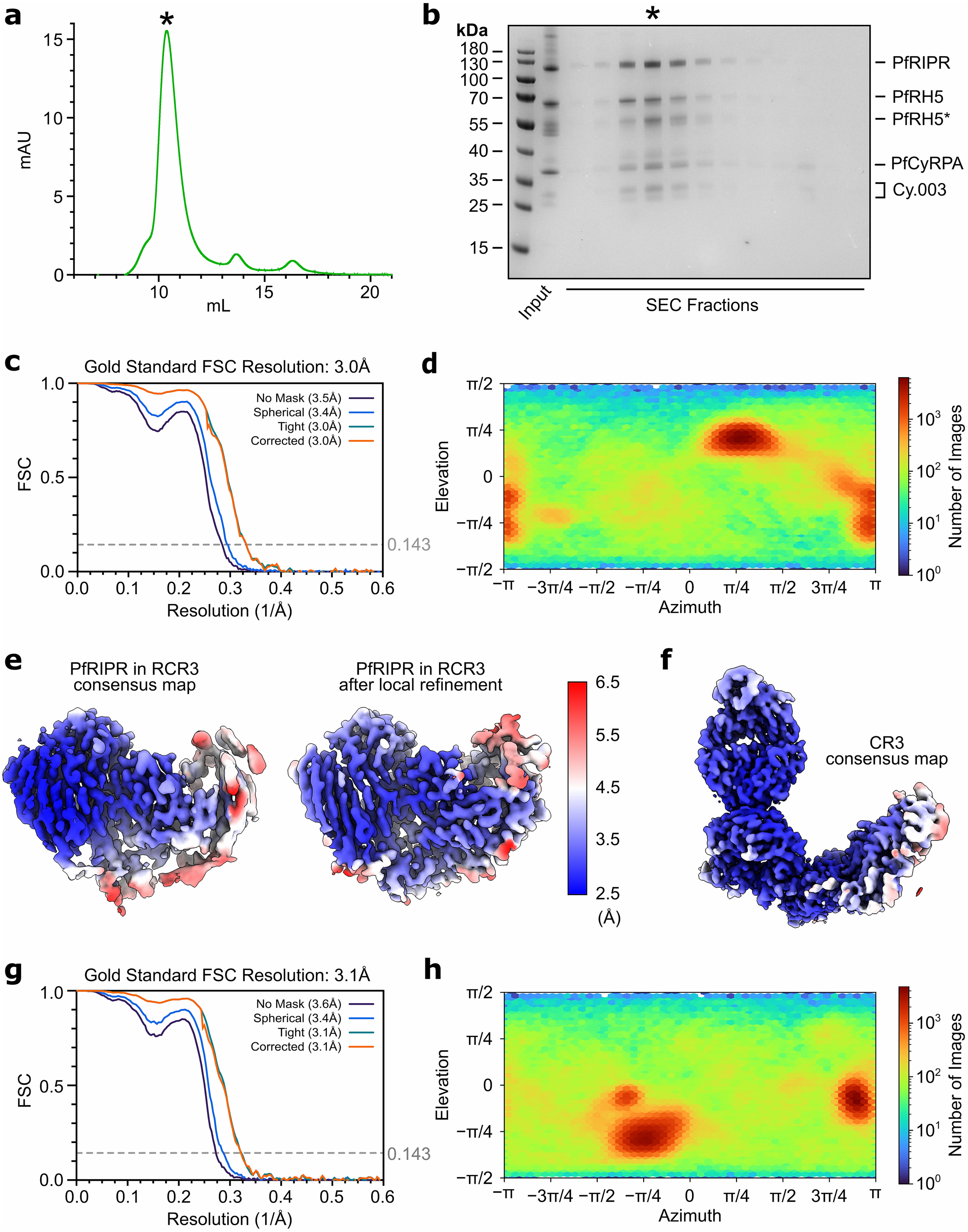

Extended Data Fig. 1 | See next page for caption.

Extended Data Fig. 1 | Purification of PfRCR-Cy.003 complex and cryo-EM processing statistics. **a**, Size exclusion chromatography profile and **b**, Reducing SDS-PAGE gel for the reconstituted PfRCR-Cy.003 complex, representative of five independent experiments. The fraction labelled with an asterisk corresponds to the region highlighted on the size exclusion chromatography profile in panel **a** containing the PfRCR-Cy.003 complex. Both full-length PfRH5 and truncated PfRH5 (PfRH5*) were observed in the purified complex. **c**, Gold-standard Fourier shell correlation curves of the consensus PfRCR-Cy.003 reconstruction. **d**, Particle view distribution of the consensus PfRCR-Cy.003 reconstruction. **e**, Map regions corresponding to PfRIPR in the consensus PfRCR-Cy.003 reconstruction and following local refinement, showing improvement in map quality. Both maps are coloured by local resolution and post-processed with DeepEMhancer. **f**, Consensus map of the PfCyRPA-PfRIPR-Cy.003 (CR3) complex, post-processed with DeepEMhancer, and coloured by local resolution as in (**e**). **g**, Gold-standard Fourier shell correlation curves of the consensus PfCyRPA-PfRIPR-Cy.003 reconstruction. **h**, Particle view distribution of the consensus PfCyRPA-PfRIPR-Cy.003 reconstruction.

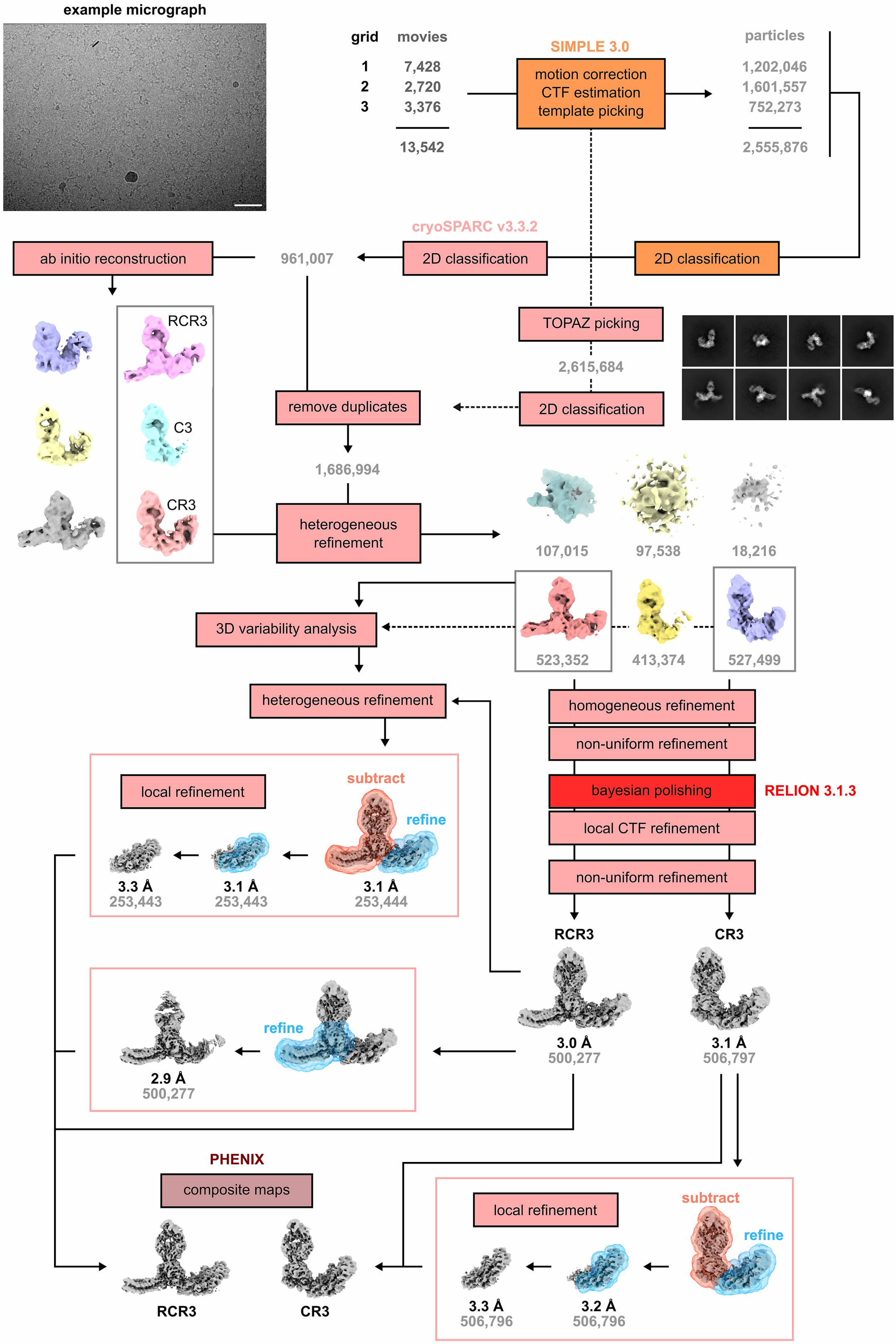

Extended Data Fig. 2 | See next page for caption.

Extended Data Fig. 2 | Workflow for cryo-EM data processing. Movies from three grids of the same PfRCR-Cy.003 sample were pre-processed separately in SIMPLE 3.0, followed by template-based particle picking in SIMPLE 3.0 and TOPAZ particle picking in cryoSPARC v3.3.2. After 2D classification and removal of duplicate particles, the cleaned particle stack was subject to heterogeneous refinement using maps for PfRCR-Cy.003 (RCR3), PfCyRPA-PfRIPR-Cy.003 (CR3) and PfCyRPA-Cy.003 (C3) complexes from *ab initio* reconstructions and three decoy volumes. Particle stacks corresponding to RCR3 and CR3 complexes were then separately refined in 3D space, then after Bayesian polishing in RELION 3.1.3 and local CTF refinement in cryoSPARC v3.3.2, subjected to a final non-uniform refinement to obtain consensus maps for each complex. Each map was further locally refined to improve the maps of PfRH5 and PfRIPR respectively using soft masks around the proteins of interest, and with signal subtraction for PfRIPR local refinements. Composite maps were generated using PHENIX. The micrograph shown is representative of 13,542 micrographs. The scale bar corresponds to 50 nm.

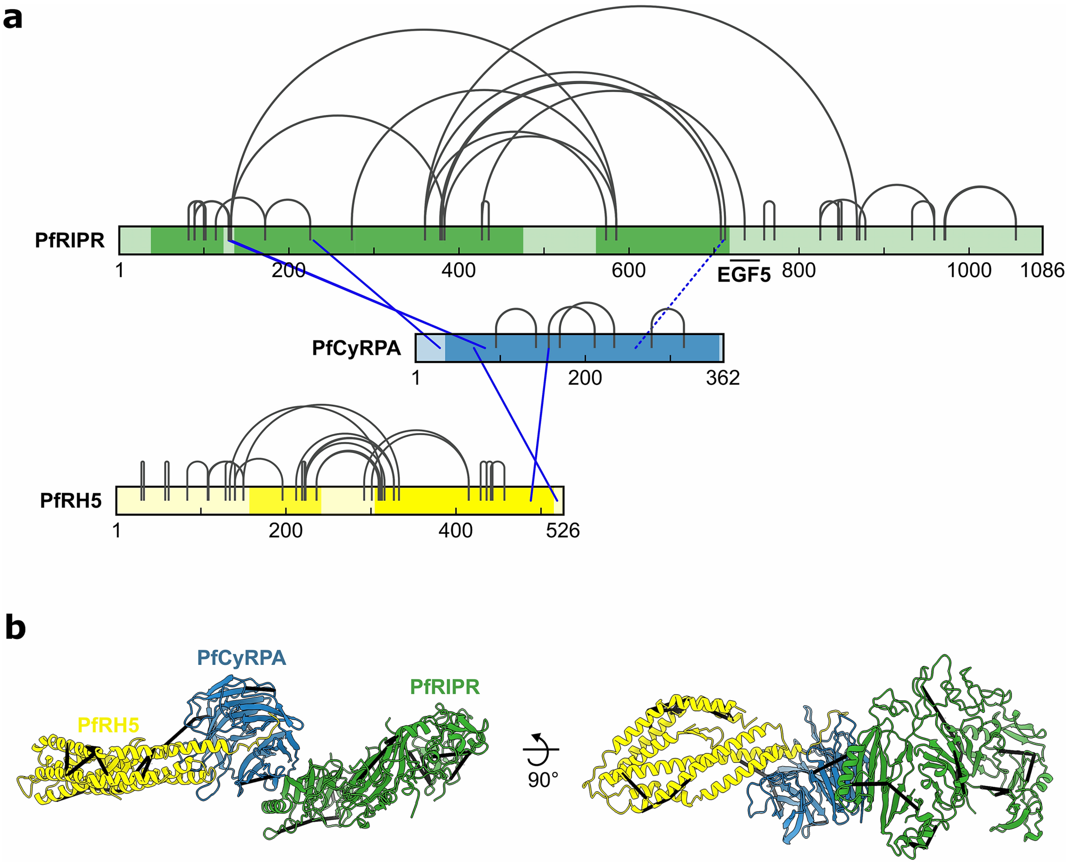

Extended Data Fig. 3 | Crosslinking mass spectrometry of the PfRCR complex. **a**, Crosslinks found between PfRIPR, PfCyRPA and PfRH5 after incubating the reconstituted PfRCR complex with the crosslinker DSSO. Inter-protein crosslinks are blue and intra-protein crosslinks are grey. Crosslinks that are inconsistent with the PfRCR complex structure (with a Cα-Cα distance greater than 35 Å) are indicated by dashed lines. The regions of PfRIPR, PfCyRPA and PfRH5 built in the PfRCR structure are highlighted by a darker tone. The location of EGF5 in PfRIPR is indicated to highlight the intra-PfRIPR crosslink supporting the proposed location of this domain in the PfRIPR structure. Prepared using xiNET[50]. **b**, Crosslinks with a Cα-Cα distance less than 35 Å mapped on to the PfRCR complex structure.

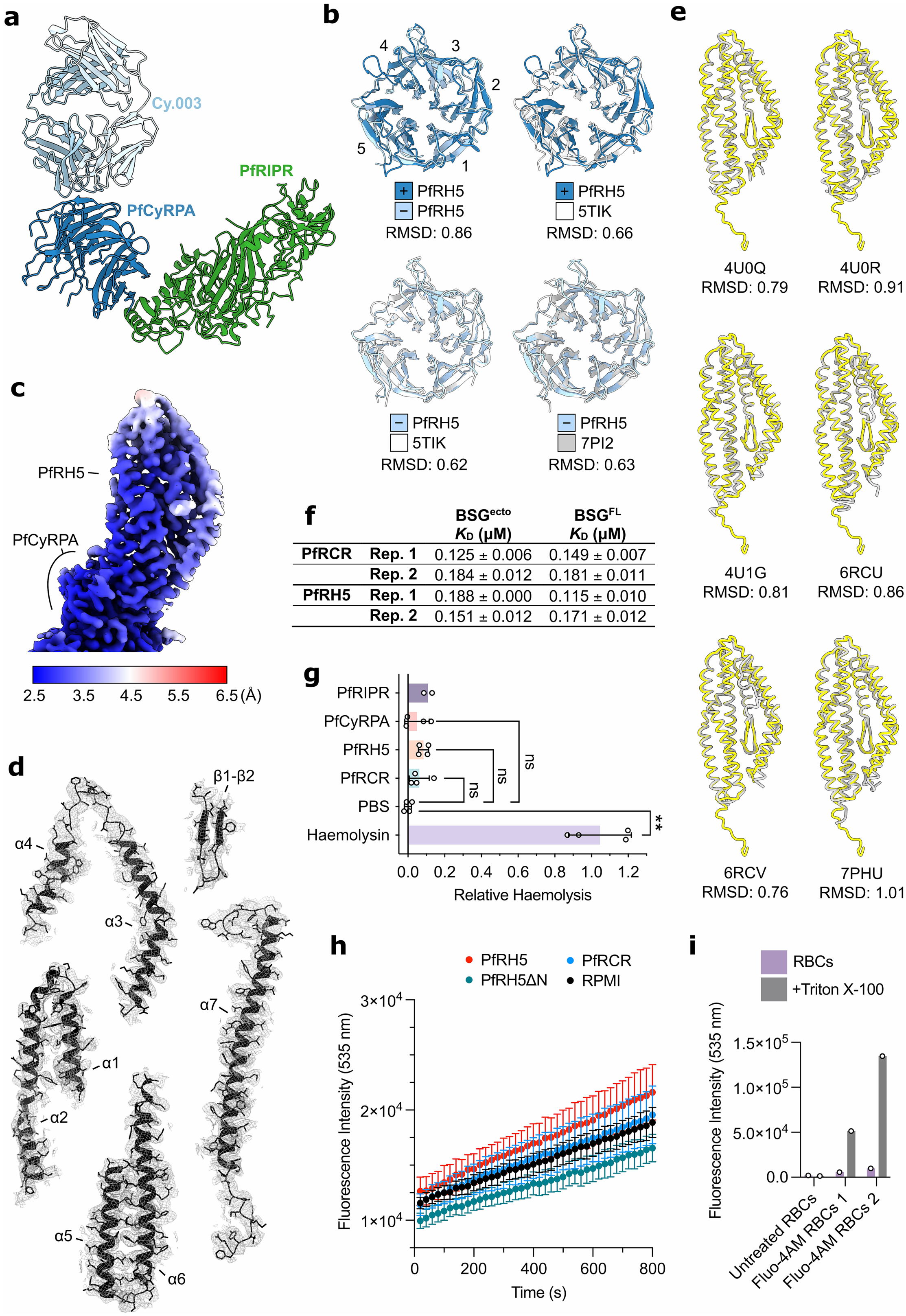

		BSG^ecto K_D (μM)	BSG^FL K_D (μM)
PfRCR	**Rep. 1**	0.125 ± 0.006	0.149 ± 0.007
	Rep. 2	0.184 ± 0.012	0.181 ± 0.011
PfRH5	**Rep. 1**	0.188 ± 0.000	0.115 ± 0.010
	Rep. 2	0.151 ± 0.012	0.171 ± 0.012

Extended Data Fig. 4 | See next page for caption.

Extended Data Fig. 4 | Comparison of PfRH5 and PfCyRPA structures and assessment of PfRH5 function. a, Structure of the PfCyRPA-PfRIPR-Cy.003 complex in cartoon representation, with PfRIPR (green), PfCyRPA (blue) and Cy.003 Fab (light blue) highlighted. **b**, Structural alignments of PfCyRPA from PfRCR-Cy.003 (dark blue), PfCyRPA-PfRIPR-Cy.003 (light blue), Cy.003-bound PfCyRPA (grey, PDB ID: 7PI2[5]), and unbound PfCyRPA (white, PDB ID: 5TIK[19]), with backbone RMSDs to each pair given below. Blades 1 through 5 are labelled. **c**, Cryo-EM map of PfRH5 following local refinement, post-processed by DeepEMhancer and coloured by local resolution. **d**, PfRH5 split into secondary structure elements, shown with their corresponding cryo-EM densities using the composite PfRCR-Cy.003 map post-processed with DeepEMhancer. **e**, Structural alignment of PfRH5 from PfRCR-Cy.003 (yellow) with crystal structures (grey) of basigin-bound (PDB ID: 4U0Q)[3] or Fab-bound PfRH5 (PDB IDs: 4U0R, 4U1G, 6RCU, 6RCV, 7PHU)[3,4]. Backbone RMSDs between PfRCR-Cy.003 and each crystal structure are given below. **f**, Binding affinity measurements for PfRCR and PfRH5 binding to basigin ectodomain (BSG^{ecto}) and full-length basigin (BSG^{FL}) determined by microscale thermophoresis. Values determined from two independently prepared samples are provided. Each of these was measured three times. **g**, Relative haemolysis following the incubation of red blood cells with 2 μM of either PfPIPR, PfCyRPA, PfRH5, PfRCR or alpha-haemolysin, or with PBS alone. Only haemolysis induced by alpha-haemolysin is significantly greater than observed with PBS alone ($p = 0.0016$ for PBS vs Haemolysin, whereas $p = 0.3207$ for PBS vs PfRH5, $p = 0.8673$ for PBS vs PfRCR, and $p > 0.9999$ for PBS vs PfCyRPA, determined using a Kruskal-Wallis one-way ANOVA adjusted for multiple comparisons using Dunn's test. N = 2 for PfRIPR (and therefore no statistical analysis has been performed) and n = 4 for all others. Individual data points, the mean +/− SD are shown. **h**, Raw fluorescence intensity measured at 535 nm after incubation of Fluo-4 loaded red blood cells (RBCs) with PfRH5, PfRH5ΔN, PfRCR, or RPMI alone. The mean +/− SEM for a technical triplicate are shown. **i**, Raw fluorescence intensity measured at 535 nm of untreated and Fluo-4AM treated RBCs, alone or following addition of 0.1% v/v Triton X-100, demonstrating successful loading of Fluo-4 (N = 1 for untreated RBCs and n = 2 for Fluo-4AM treated RBCs).

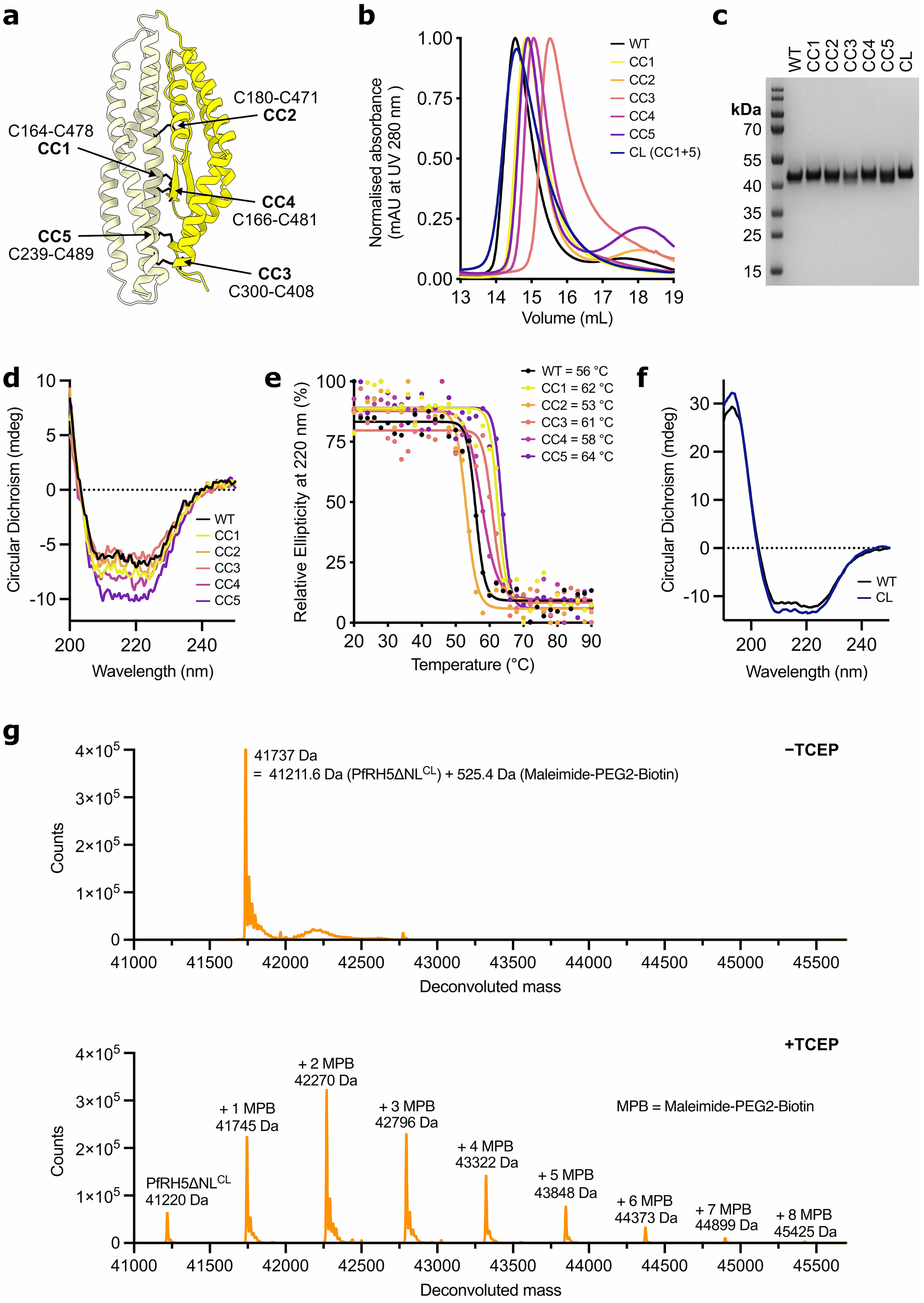

Extended Data Fig. 5 | See next page for caption.

Extended Data Fig. 5 | Design, expression and characterisation of cysteine-locked PfRH5. a, PfRH5 in cartoon showing the location of the five designed disulphide bonds (CC1 to CC5, black sticks), joining the N-terminal (dark yellow) and C-terminal (light yellow) halves of PfRH5. **b**, Gel filtration traces of purified wild-type PfRH5ΔNL (a construct lacking the unstructured N-terminus and α2-α3 loop of PfRH5[3]) and the cysteine-locked PfRH5 designs (CC1 to CC5) following expression in *Drosophila* S2 cells. **c**, SDS-PAGE gel of purified wild-type and single cysteine-locked variants (CC1 to CC5) and the double cysteine-locked (PfRH5^{CL}, which combines crosslinks CC1 and CC5) version of PfRH5ΔNL. CC1 to CC5 were each expressed and purified once, while PfRH5^{CL} is representative of 3 independent samples. **d**, Single circular dichroism traces of wild-type and cysteine-locked variants of PfRH5ΔNL at 20 °C from their respective temperature ramps. **e**, Relative ellipticity at 220 nm versus temperature, and the calculated melting temperature of wild-type and cysteine-locked variants of PfRH5ΔNL. **f**, Circular dichroism traces of purified wild-type and the double cysteine-locked PfRH5ΔNL (PfRH5ΔNL^{CL}). **g**, Intact mass spectrometry analysis of PfRH5ΔNL^{CL} following maleimide-PEG-biotin labelling in the absence (top) and the presence of TCEP (bottom). Unlabelled PfRH5ΔNL^{CL} has a theoretical mass of 41211.6 Da and +526 Da mass differences correspond to a maleimide-PEG2-biotin addition to cysteine residues.

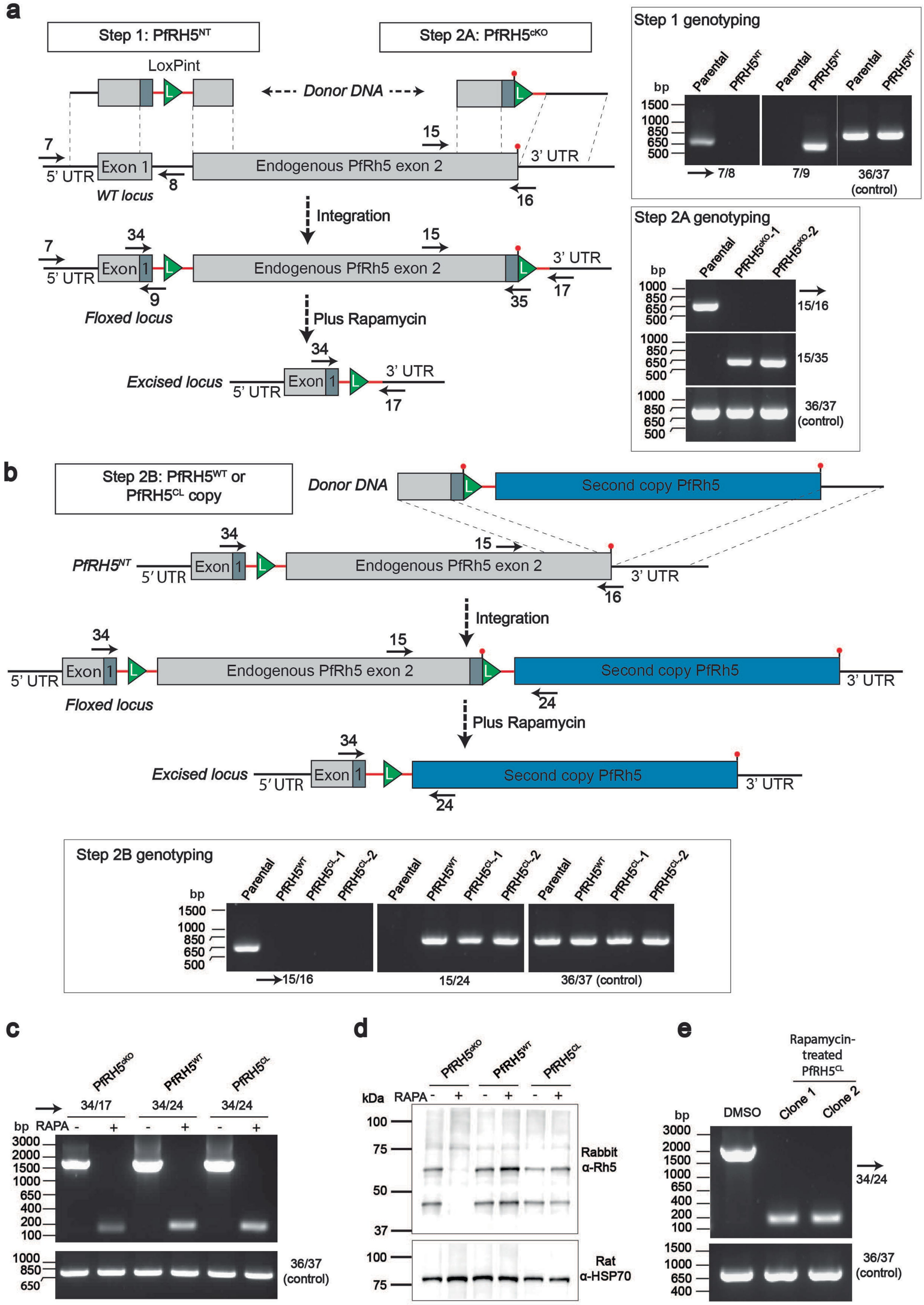

Extended Data Fig. 6 | See next page for caption.

Extended Data Fig. 6 | Generation of PfRH5 conditional knockout and complemented parasites. **a**, Schematic illustrating generation of transgenic rapamycin-inducible PfRH5^{cKO} line through the successive introduction of 5′ *LoxPint* (Step 1, generating line PfRH5^{NT}) followed by 3′ *LoxPint* site (Step 2 A), resulting in floxed exon 2 of *PfRh5* (line PfRH5^{cKO}). Genotyping PCRs are shown (inset on right). One clone of PfRH5^{NT} and two clones of PfRH5^{cKO} parasites were generated. Solid black arrows indicate position of primers used to screen by PCR for integration of *LoxP* sites, which was done once. Primers are numbered as in Supplementary Table 1. **b**, Schematic illustrating the introduction of a second, complementary copy of *PfRH5* (either PfRH5^{WT} or PfRH5^{CL}) 3′ to endogenous *PfRH5*. The donor DNA included 548 bp of 3′ end of endogenous *PfRH5* followed by a small recodonised sequence, part of *LoxPint*, the second copy, and finally, 591 bp of endogenous 3′UTR. This design allowed for inducible complementation such that after rapamycin induced excision, only the complementary copy of *PfRH5* was expressed. PCR genotyping of Step 2B is shown in inset. One clone of PfRH5^{WT} and two clones of PfRH5^{CL} parasites were generated. For schematics in both **a** and **b**, green triangles represent *LoxP* DNA sequence; red lines represent *sera2* intron sequence; dark grey shaded boxes represent recodonised pieces of DNA. **c**, Genotyping PCR demonstrating that rapamycin induced excision of endogenous *PfRH5* exon 2. Data shown is representative of two biological repeats. **d**, Anti-PfRH5 western blotting demonstrating ablation of PfRH5 expression for rapamycin treated PfRH5^{cKO} parasites or expression of a complementary copy of *PfRH5* for PfRH5^{WT} and PfRH5^{CL} lines. Hsp70 was used as a loading control. Data shown is representative of three biological repeats. **e**, Rapamcyin treated PfRH5^{CL} parasites could be cloned by limiting dilution and maintained in culture. Primers used in PCR genotyping are listed in Supplementary Table 1 and the expected PCR product sizes in Supplementary Table 2. This was done once. For each set of PCR reactions, control primers 36/37 were used to amplify a 737 bp product from the *PfRON2* locus.

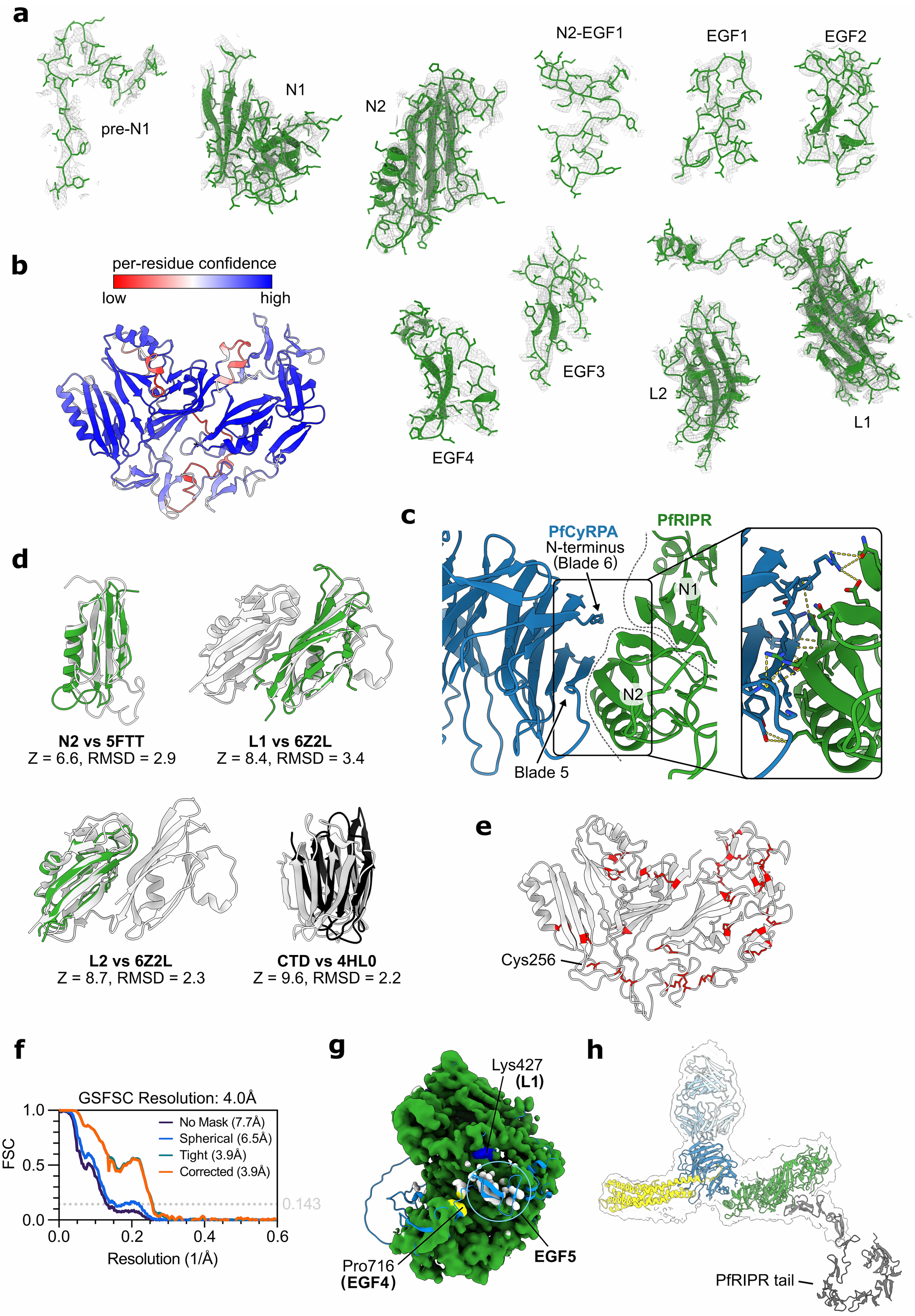

Extended Data Fig. 7 | See next page for caption.

Extended Data Fig. 7 | The PfRIPR core and generating a composite model of full-length PfRIPR. a, Domains of PfRIPR with their corresponding cryo-EM density using the PfRCR-Cy.003 composite map post-processed with DeepEMhancer. **b**, AlphaFold2 prediction of PfRIPR residues 19–716 (except 484–548) coloured by pLDDT score. The regions of low confidence in this model correlate with those that required de novo building guided by the AlphaFold2 prediction. **c**, The interface between PfRIPR and PfCyRPA comprises backbone and side chain interactions between residues of domains N1 and N2 of PfRIPR (green) and blades 5 and 6 of PfCyRPA (blue). Each are shown as cartoons with side chains of interacting residues (detailed in Extended Data Table 4) shown as sticks in the expanded section. Hydrogen bonds between residues are shown in yellow. **d**, Structural alignment of PfRIPR domains and their structural homologues with their DALI Z scores and RMSD scores. Structural homologues are identified by their PDB codes: 5FTT (lectin domain of Lactrophilin 3), 6Z2L (PfP113) and 4HL0 (Galectin). **e**, The PfRIPR core contains 23 disulphide bonds and one free cysteine (Cys256). Cysteine residues are shown as red sticks. **f**, Gold standard Fourier shell correlation (GSFSC) curves for the PfRCR-Cy.003 map containing additional density for the start of the PfRIPR tail. **g**, The PfRIPR portion of the composite PfRCR-Cy.003 map coloured green where a model of the PfRIPR core has been built. Uninterpretable density (coloured white) is observed in this map beyond domain EGF4 at Pro716 (yellow). An AlphaFold2 model of PfRIPR truncated after EGF5 (residues 20–769, light blue cartoon) predicts that this likely corresponds to EGF5. This is further supported by a chemical crosslink found between Lys736 of domain EGF5 and Lys427 of domain L1 (dark blue) in XL-MS analysis of the PfRCR complex (Extended Data Fig. 3). **h**, To generate a composite model of full-length PfRIPR, the AlphaFold 2 prediction of the PfRIPR tail (residues 717–1086) was docked onto the PfRIPR core using the 4.0 Å PfRCR-Cy.003 map containing additional PfRIPR density as a guide.

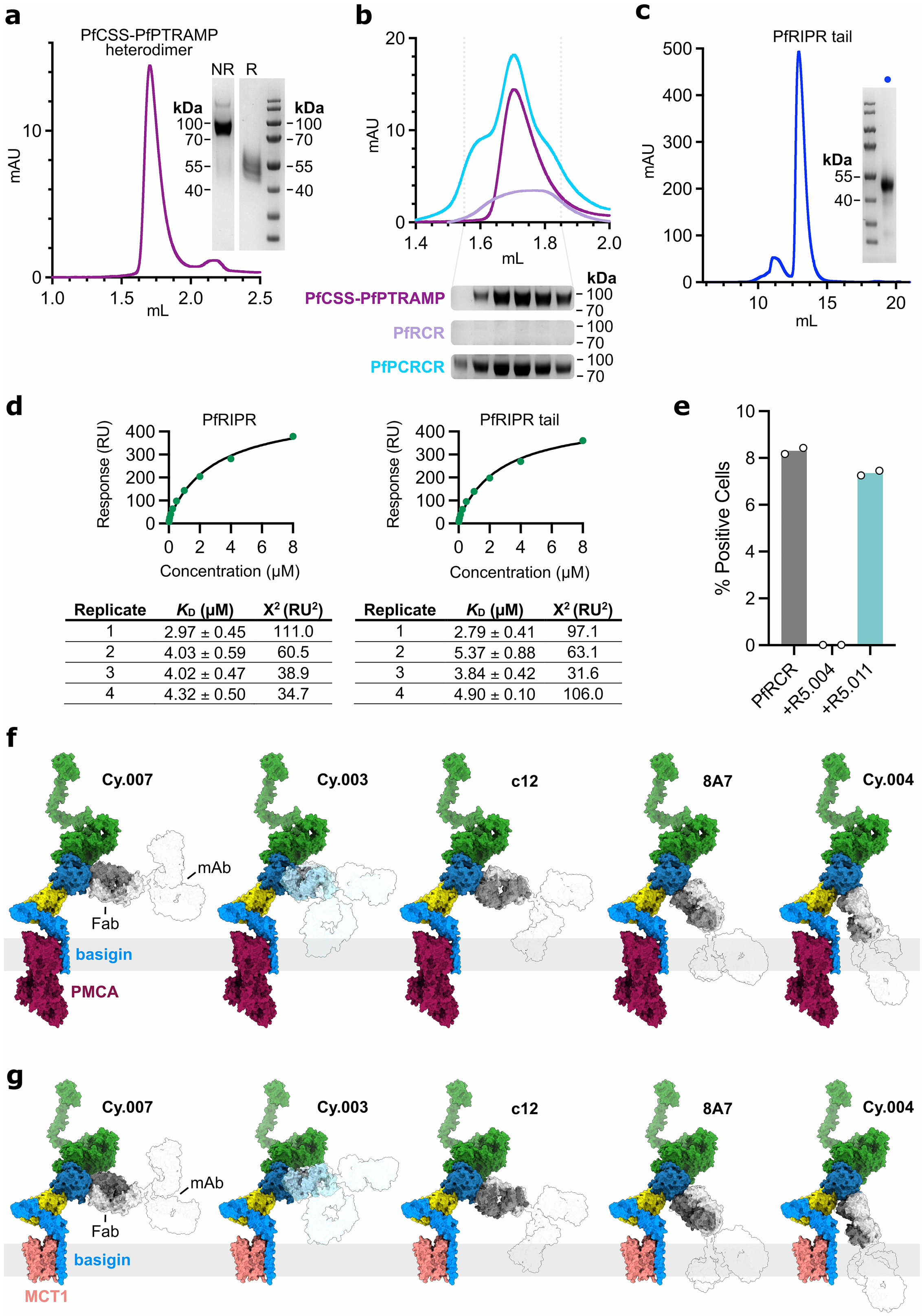

Replicate	K_D (μM)	X^2 (RU^2)
1	2.97 ± 0.45	111.0
2	4.03 ± 0.59	60.5
3	4.02 ± 0.47	38.9
4	4.32 ± 0.50	34.7

Replicate	K_D (μM)	X^2 (RU^2)
1	2.79 ± 0.41	97.1
2	5.37 ± 0.88	63.1
3	3.84 ± 0.42	31.6
4	4.90 ± 0.10	106.0

Extended Data Fig. 8 | See next page for caption.

Extended Data Fig. 8 | PfRIPR tail interacts with the PfCSS-PfPTRAMP complex, and the mapping of anti-PfCyRPA antibodies. a, Gel filtration trace of the PfCSS-PfPTRAMP heterodimer with an SDS-PAGE gel inset right. SDS-PAGE fractions are shown for non-reduced (NR) and reduced (R) samples of the disulphide-linked heterodimer. Representative of three independent experiments. **b**, Gel filtration traces for PfCSS-PTRAMP complex (dark purple), PfRCR (light purple) and the mixture of the two complexes (blue). Underneath non-reducing SDS-PAGE gels show the corresponding fractions for the location of PfCSS-PfPTRAMP from the three experiments. Traces and gels are representative of two independent analyses. **c**, Gel filtration trace of recombinantly expressed PfRIPR tail with reducing SDS-PAGE gel of isolated PfRIPR tail shown inset right, representative of three independent samples. **d**, Representative steady state fit analysis of PfCSS-PfPTRAMP complex binding to full-length PfRIPR and PfRIPR tail by SPR. Binding analysis was completed four times. Inset below are the estimated binding affinity (K_D) and the Chi^2 fit for each repeat. **e**, FACS-based analysis of the binding of PfRCR complex to human erythrocytes in the presence of PfRH5-targeting antibodies R5.004 and R5.011. In each case, PfRCR was detected using an anti-C-tag nanobody targeting the affinity tag of the complex. Binding of the PfRCR complex is unaffected by the presence of R5.011. N = 2, individual data points, the mean +/- SD are shown. **f**, Composite model showing structural alignment of anti-PfCyRPA antibodies on to the PfRCR complex when bound to PMCA-bound basigin on the erythrocyte surface, with the rest of the antibodies modelled as faint silhouettes. Generated through alignment of the PfRCR-Cy.003 complex, Fab-PfCyRPA crystal structures (PDB IDs: 7PHV, 5EZO, 5TIH and 7PHW)[5,19,20], an intact IgG crystal structure (PDB ID: 1IGT), and PMCA-bound basigin (PDB ID: 6A69[34]). **g**, As in (**f**) except when PfRCR is bound to MCT1-bound basigin (PDB ID: 7CKR[33]).

Extended Data Table 1 | Cryo-EM data collection, refinement, and validation statistics of PfRCR-Cy.003

	PfRCR-Cy.003				
	Composite map (EMDB-16569) (PDB-8CDD)	**Consensus refinement** (EMDB-16637)	**Local PfRH5 refinement** (EMDB-16638)	**Local PfRIPR refinement** (EMDB-16639)	**With tail density refinement** (EMDB-16640)
Data collection and processing					
Microscope		Titan Krios			
Detector		Gatan K3 with 20 eV Energy Filter			
Magnification		58,149			
Voltage (kV)		300			
Electron exposure (e^-/Å^2)		48.97			
Defocus range (μm)		-1.0 to -3.0			
Pixel size (Å)		0.832			
Symmetry imposed		C1	C1	C1	C1
Initial particle images (no.) [a]		2,615,684	2,615,684	2,615,684	2,615,684
Final particle images (no.)		500,277	500,277	253,444	62,817
Map resolution (Å)		3.0	2.9	3.3	4.0
FSC threshold		0.143	0.143	0.143	0.143
Map resolution range (Å)		2.5-6.3	2.6-5.8	2.8-10.5	3.3-13.6
FSC threshold		0.5	0.5	0.5	0.5
Map sharpening B-factor (Å^2)	n/a [b]	n/a [c]	n/a [c]	n/a [c]	n/a [d]
Map combination method	PHENIX				
Maps combined (EMDB codes)	EMDB-16637, EMDB-16638, EMDB-16639				
Refinement					
Initial model used (PDB code)	4U0Q, 7PI2, AlphaFold2, *de novo*				
Model resolution (Å)	3.4				
FSC threshold	0.5				
Model composition					
Non-hydrogen atoms	13140				
Protein residues	1633				
Ligands	n/a				
B factors (Å^2)					
Protein	156.5				
Ligands	n/a				
R.m.s deviations					
Bond length (Å)	0.003				
Bond angles (°)	0.658				
Validation					
Molprobity score	2.46				
Clash score	13.80				
Poor rotamers (%)	3.67				
Ramachandran plot					
Favored (%)	94.37				
Allowed (%)	5.63				
Outliers (%)	0				
Model vs. data fit					
CC (mask)	0.80				
CC (box)	0.86				

[a] - TOPAZ picked particles, [b] – composite of maps [c] – DeepEMhancer postprocessed, [d] – no sharpening performed.

Extended Data Table 2 | PfRCR mass spectrometry crosslinks

Type	Protein 1	LinkPos1	Protein 2	LinkPos2	Distance (Å)
Intra-protein	PfRIPR	100	PfRIPR	89	12.5
Intra-protein	PfRIPR	100	PfRIPR	82	6.5
Intra-protein	PfRIPR	102	PfRIPR	82	7.2
Intra-protein	PfRIPR	129	PfRIPR	89	n/a
Intra-protein	PfRIPR	130	PfRIPR	89	n/a
Intra-protein	PfRIPR	172	PfRIPR	114	14.6
Intra-protein	PfRIPR	172	PfRIPR	225	14.3
Intra-protein	PfRIPR	274	PfRIPR	585	33.2
Intra-protein	PfRIPR	360	PfRIPR	573	14.7
Intra-protein	PfRIPR	360	PfRIPR	713	15.5
Intra-protein	PfRIPR	383	PfRIPR	585	11.8
Intra-protein	PfRIPR	383	PfRIPR	132	n/a
Intra-protein	PfRIPR	427	PfRIPR	435	16.4
Intra-protein	PfRIPR	585	PfRIPR	132	n/a
Intra-protein	PfRIPR	708	PfRIPR	378	11.8
Intra-protein	PfRIPR	708	PfRIPR	380	15.8
Intra-protein	PfRIPR	736	PfRIPR	427	n/a
Intra-protein	PfRIPR	759	PfRIPR	771	n/a
Intra-protein	PfRIPR	825	PfRIPR	847	n/a
Intra-protein	PfRIPR	825	PfRIPR	878	n/a
Intra-protein	PfRIPR	850	PfRIPR	846	n/a
Intra-protein	PfRIPR	868	PfRIPR	360	n/a
Intra-protein	PfRIPR	933	PfRIPR	959	n/a
Intra-protein	PfRIPR	959	PfRIPR	871	n/a
Intra-protein	PfRIPR	1055	PfRIPR	971	n/a
Intra-protein	PfRIPR	1055	PfRIPR	972	n/a
Inter-protein	PfRIPR	129	PfCyRPA	82	n/a
Inter-protein	PfRIPR	132	PfCyRPA	82	n/a
Intra-protein	PfCyRPA	142	PfCyRPA	95	15.2
Intra-protein	PfCyRPA	170	PfCyRPA	234	8.8
Intra-protein	PfCyRPA	211	PfCyRPA	157	13.2
Intra-protein	PfCyRPA	278	PfCyRPA	316	15.0
Inter-protein	PfCyRPA	29	PfRIPR	229	n/a
Inter-protein	PfCyRPA	69	PfRH5	519	n/a
Inter-protein	PfCyRPA	157	PfRH5	488	17.4
Inter-protein	PfCyRPA	259	PfRIPR	711	88.3
Intra-protein	PfRH5	33	PfRH5	30	n/a
Intra-protein	PfRH5	58	PfRH5	62	n/a
Intra-protein	PfRH5	108	PfRH5	84	n/a
Intra-protein	PfRH5	134	PfRH5	313	n/a
Intra-protein	PfRH5	140	PfRH5	129	n/a
Intra-protein	PfRH5	150	PfRH5	333	n/a
Intra-protein	PfRH5	150	PfRH5	108	n/a
Intra-protein	PfRH5	150	PfRH5	109	n/a
Intra-protein	PfRH5	196	PfRH5	140	n/a
Intra-protein	PfRH5	219	PfRH5	223	6.8
Intra-protein	PfRH5	219	PfRH5	222	5.4
Intra-protein	PfRH5	223	PfRH5	316	12.7
Intra-protein	PfRH5	309	PfRH5	236	14.5
Intra-protein	PfRH5	311	PfRH5	236	13.4
Intra-protein	PfRH5	327	PfRH5	223	14.7
Intra-protein	PfRH5	327	PfRH5	222	15.8
Intra-protein	PfRH5	327	PfRH5	212	13.9
Intra-protein	PfRH5	415	PfRH5	292	n/a
Intra-protein	PfRH5	415	PfRH5	301	n/a
Intra-protein	PfRH5	429	PfRH5	436	11.1
Intra-protein	PfRH5	441	PfRH5	457	13.3
Intra-protein	PfRH5	443	PfRH5	436	11.4

Crosslinks found between PfRIPR, PfCyRPA and PfRH5 after incubating the PfRCR complex with the crosslinker DSSO. LinkPos1 and LinkPos2 refer to the residues crosslinked from each protein. Where possible, the Cα-Cα distance measured between residues in the PfRCR structure is given.

Extended Data Table 3 | Cryo-EM data collection, refinement, and validation statistics for PfCyRPA-PfRIPR-Cy.003

	PfCyRPA-PfRIPR-Cy.003		
	Composite map (EMDB-16570) (PDB-8CDE)	**Consensus refinement** (EMDB-16636)	**Local PfRIPR refinement** (EMDB-16635)
Data collection and processing			
Microscope		Titan Krios	
Detector		Gatan K3 with 20 eV Energy Filter	
Magnification		58,149	
Voltage (kV)		300	
Electron exposure (e^{-}/Å^{2})		48.97	
Defocus range (μm)		-1.0 to -3.0	
Pixel size (Å)		0.832	
Symmetry imposed		C1	C1
Initial particle images (no.) [a]		2,615,684	2,615,684
Final particle images (no.)		506,797	500,796
Map resolution (Å)		3.1	3.3
FSC threshold		0.143	0.143
Map resolution range (Å)		2.6-6.9	2.6-8.8
FSC threshold		0.5	0.5
Map sharpening B-factor (Å^{2})	n/a [b]	n/a [c]	n/a [c]
Map combination method	PHENIX		
Maps combined (EMDB codes)	EMDB-16635, EMDB-16636		
Refinement			
Initial model used (PDB code)	7PI2, 8CDD		
Model resolution (Å)	3.6		
FSC threshold	0.5		
Model composition			
Non-hydrogen atoms	10465		
Protein residues	1317		
Ligands	n/a		
B factors (Å^{2})			
Protein	171.9		
Ligands	n/a		
R.m.s deviations			
Bond length (Å)	0.003		
Bond angles (°)	0.713		
Validation			
Molprobity score	2.38		
Clash score	8.14		
Poor rotamers (%)	4.02		
Ramachandran plot			
Favored (%)	92.12		
Allowed (%)	7.88		
Outliers (%)	0		
Model vs. data fit			
CC (mask)	0.74		
CC (box)	0.82		

[a] - TOPAZ picked particles, [b]– composite of maps [c] – DeepEMhancer postprocessed.

Extended Data Table 4 | Interface residues of the PfRCR complex

	PfCyRPA				PfRIPR			
Chain	**Residue**	**Group**	**Location**	**Chain**	**Residue**	**Group**	**Location**	**Interaction**
B	Ile35	backbone	Blade 6	A	His191	side chain	N2 strand	hydrogen bond
B	Arg36	side chain	Blade 6	A	Asn66	side chain	N1 strand	hydrogen bond
		side chain	Blade 6	A	Glu166	side chain	N2 strand	salt bridge
B	Thr37	backbone	Blade 6	A	Gln241	side chain	N2 strand	hydrogen bond
B	Leu39		Blade 6					hydrophobic
B	Glu302	side chain	Blade 5	A	Lys208	side chain	N2 helix	salt bridge
B	Tyr304		Blade 5					hydrophobic
B	Asn309	backbone	Blade 5	A	Gln200	side chain	N2 helix	hydrogen bond
B	Glu310	backbone	Blade 5	A	Gln200	side chain	N2 helix	hydrogen bond
		backbone	Blade 5	A	Thr194	backbone	N2 strand	hydrogen bond
		side chain	Blade 5	A	His193	side chain	N2 strand	hydrogen bond
B	Asn311	side chain	Blade 5	A	His193	side chain	N2 strand	salt bridge
B	Ser312	backbone	Blade 5	A	Val192	backbone	N2 strand	hydrogen bond
B	Ile313	backbone	Blade 5	A	His191	backbone	N2 strand	hydrogen bond
								hydrophobic
B	Leu314	backbone	Blade 5	A	Val190	backbone	N2 strand	hydrogen bond
B	Lys316	backbone	Blade 5	A	Arg188	backbone	N2 strand	hydrogen bond
		side chain	Blade 5			side chain	N2 strand	hydrogen bond
B	Pro317	backbone	Blade 5	A	Arg188	side chain	N2 strand	hydrogen bond
B	Asn352	side chain	Blade 6	A	Arg188	side chain	N2 strand	hydrogen bond

	PfCyRPA				PfRH5			
Chain	**Residue**	**Group**	**Location**	**Chain**	**Residue**	**Group**	**Location**	**Interaction**
B	Asn45	backbone	Blade 1	C	Gln516	side chain	C-terminal tail	hydrogen bond
B	Pro47	side chain	Blade 1	C	Tyr514	side chain	C-terminal tail	pi stack
B	Ile49	backbone	Blade 1	C	Val508	backbone	C-terminal tail	hydrogen bond
		side chain						hydrophobic
B	Arg50	side chain	Blade 1	C	Asp507	side chain	C-terminal tail	salt bridge
		side chain		C	Met503	backbone	α7	hydrogen bond
B	Arg102	side chain	Blade 2	C	Asp507	side chain	C-terminal tail	salt bridge
B	Glu123	side chain	Blade 2	C	His496	side chain	α7	salt bridge
		side chain						hydrophobic
B	Phe124	side chain	Blade 2					hydrophobic
B	Leu160	side chain	Blade 3					hydrophobic
B	Leu161	backbone	Blade 3	C	Gln502	side chain	α7	hydrogen bond
B	Pro184	side chain	Blade 3					hydrophobic
B	Tyr185	side chain	Blade 3	C	Asn491	backbone	α7	hydrogen bond
B	Phe187	side chain	Blade 3					hydrophobic
B	Lys188	side chain	Blade 3	C	Asp382	side chain	α5	salt bridge
		side chain		C	Asn385	side chain	α5	hydrogen bond
B	Phe226	side chain	Blade 4					hydrophobic
B	Phe227	backbone	Blade 4	C	Gln502	side chain	α7	hydrogen bond
B	Asp245	backbone	Blade 4	C	Asn396	side chain	α5	hydrogen bond
		side chain		C	Lys399	side chain	α5	salt bridge
B	Ile247	side chain	Blade 4					hydrophobic
B	Tyr328	side chain	Blade 6					hydrophobic
B	Gln348	side chain	Blade 6	C	Glu513	side chain	C-terminal tail	hydrogen bond
		side chain		C	Lys511	side chain	C-terminal tail	hydrogen bond
				C	Ile386	side chain	α5	hydrophobic
				C	Leu392	side chain	α5	hydrophobic
				C	Leu393	side chain	α5	hydrophobic
				C	His495	side chain	α7	hydrophobic
				C	Ile498	side chain	α7	hydrophobic
				C	Leu501	side chain	α7	hydrophobic
				C	Phe505	side chain	α7	hydrophobic
				C	Pro509	side chain	C-terminal tail	hydrophobic
				C	Ile510	side chain	C-terminal tail	hydrophobic

nature portfolio

Corresponding author(s): Matthew K. Higgins

Last updated by author(s): 20-10-2023

Reporting Summary

Nature Portfolio wishes to improve the reproducibility of the work that we publish. This form provides structure for consistency and transparency in reporting. For further information on Nature Portfolio policies, see our Editorial Policies and the Editorial Policy Checklist.

Statistics

For all statistical analyses, confirm that the following items are present in the figure legend, table legend, main text, or Methods section.

n/a	Confirmed	
☐	☒	The exact sample size (*n*) for each experimental group/condition, given as a discrete number and unit of measurement
☐	☒	A statement on whether measurements were taken from distinct samples or whether the same sample was measured repeatedly
☐	☒	The statistical test(s) used AND whether they are one- or two-sided *Only common tests should be described solely by name; describe more complex techniques in the Methods section.*
☒	☐	A description of all covariates tested
☒	☐	A description of any assumptions or corrections, such as tests of normality and adjustment for multiple comparisons
☐	☒	A full description of the statistical parameters including central tendency (e.g. means) or other basic estimates (e.g. regression coefficient) AND variation (e.g. standard deviation) or associated estimates of uncertainty (e.g. confidence intervals)
☐	☒	For null hypothesis testing, the test statistic (e.g. *F*, *t*, *r*) with confidence intervals, effect sizes, degrees of freedom and *P* value noted *Give P values as exact values whenever suitable.*
☒	☐	For Bayesian analysis, information on the choice of priors and Markov chain Monte Carlo settings
☒	☐	For hierarchical and complex designs, identification of the appropriate level for tests and full reporting of outcomes
☒	☐	Estimates of effect sizes (e.g. Cohen's *d*, Pearson's *r*), indicating how they were calculated

Our web collection on statistics for biologists contains articles on many of the points above.

Software and code

Policy information about availability of computer code

Data collection	Software used for data collection are commercially available or openly accessible. Cryo-EM data were collected using EPU version 2.9.0.1519 (Thermo Fisher). Flow cytometry to measure parasite parasitaemia was collected using BD FACSDiva™ Software version 9, and for erythrocyte binding assays using ProSort™ Software (Bio-Rad). SPR data were collected using T200 Biacore Software version 2.0 (GE Healthcare). CD data were collected using Spectra Manager Version 2 (Jasco). Live cell imaging of parasite invasion for calcium flux assays was acquired using the NIS Advanced Research software package (Nikon). In-plate calcium flux assay data were acquired using CLARIOstar® software version v5.6.0 R2. Design and modeling of cysteine-locked versions of PfRH5 were performed using Rosetta version 2019.35.
Data analysis	Data analysis was performed as described in the methods section using commercially available or openly accessible software. Software used for cryo-EM data processing (SIMPLE 3.0, cryoSPARC v3.3.2, RELION 3.1.3, and DeepEMhancer v1.0.0) are standard and freely available to academic users. Model building and refinement was performed with COOT version ccp4-8.0, ISOLDE v1.5 and PHENIX v1.20.1-4487. A local installation of open source AlphaFold v2.1.1 was used for structure prediction. Chimera v1.16 and ChimeraX v1.4 and 1.5 were used for structure visualisation. GraphPad Prism version 8.4.3 and 9.2.0 was used to generate graphs and for statistical tests. T200 Biacore Evaluation software v1.0 is provided with the Biacore SPR machine and is standard in the field. Proteome Discoverer 2.5 and XlinkX node (Thermo Fisher) were used for cross-linking mass spectrometry analysis, and xiNET (https://https://crosslinkviewer.org/) was used for visualisation of crosslinks. Flow cytometry to measure parasite parasitaemia and erythrocyte binding was analysed using FlowJo version 10. Live cell imaging was processed using the NIS Advanced Research software package (Nikon).

For manuscripts utilizing custom algorithms or software that are central to the research but not yet described in published literature, software must be made available to editors and reviewers. We strongly encourage code deposition in a community repository (e.g. GitHub). See the Nature Portfolio guidelines for submitting code & software for further information.

Data

Policy information about availability of data

All manuscripts must include a data availability statement. This statement should provide the following information, where applicable:

- Accession codes, unique identifiers, or web links for publicly available datasets
- A description of any restrictions on data availability
- For clinical datasets or third party data, please ensure that the statement adheres to our policy

Cryo-EM maps for PfRCR-Cy.003 are available from the Electron Microscopy Data Bank under accession codes EMDB-16569, EMDB-16637, EMDB-16638, EMDB-16639 and EMDB-16640, and its coordinates from the Protein Data Bank under accession code 8CDD. Cryo-EM maps for PfCyRPA-PfRIPR-Cy.003 are available under accession codes EMDB-16570, EMDB-16636 and EMDB-16635, and its coordinates from the Protein Data Bank under accession code 8CDE. In this study, previously published structures have been used for structural analysis; these can be found in the Protein Data Bank under accession codes 1IGT, 4HL0, 4U0Q, 4U0R, 4U1G, 5EZO, 5FTT, 5TIH, 5TIK, 6A69, 6RCU, 6RCV, 6Z2L, 7CKR, 7PHU, 7PHV, 7PHW, 7PI2 and 7UNY. Uncropped gels and source data for all graphs generated in this study are provided in Supplementary Figures and “source_data.xlsx” respectively. The "Rosetta Disulfidize" and "Rosetta FastRelax" scripts used to design cysteine-locked version of PfRH5 in this manuscript are also provided in "source_data.xlsx".

Human research participants

Policy information about studies involving human research participants and Sex and Gender in Research.

Reporting on sex and gender	N/A
Population characteristics	N/A
Recruitment	N/A
Ethics oversight	N/A

Note that full information on the approval of the study protocol must also be provided in the manuscript.

Field-specific reporting

Please select the one below that is the best fit for your research. If you are not sure, read the appropriate sections before making your selection.

☒ Life sciences ☐ Behavioural & social sciences ☐ Ecological, evolutionary & environmental sciences

For a reference copy of the document with all sections, see nature.com/documents/nr-reporting-summary-flat.pdf

Life sciences study design

All studies must disclose on these points even when the disclosure is negative.

Sample size	Sample sizes are described in figure legends and methods. No statistical method was used to predetermine sample size. Quantitative experiments were typically repeated in technical triplicate. Sample sizes for each experiment were chosen to be consistent with the field norms. For flow cytometry experiments, we collected at least three biological replicates, each with three technical replicates for each data point. FACS analyses to determine parasitaemia counts measured the numbers of parasite-infected cells in a total of 30,000 red blood cells. Since parasitaemia values ranged from 0.5-7.5%, this was considered sufficient to provide statistically robust measurements of parasitaemia. For imaging, at least 40 events resulting from 20-25 schizont egresses were analysed, as per field norms (e.g., https://doi.org/10.1038/s41467-023-40357-z) and to obtain data sufficient to observe statistical differences for control experiments.
Data exclusions	For both PfRH5 and PfRCR binding analyses by microscale thermophoresis, traces from concentrations greater than 2 µM for full-length basigin measurements and greater than 5 µM for basigin ectodomain measurements were excluded due to significant variations in raw fluorescence. As is standard for cryo-EM workflows, particles not contributing to classes of interest were excluded from the final reconstructions.
Replication	The number of repeats for each relevant experiment are given in figure legends and the methods. Typically, experiments were performed in independent technical triplicates. Flow cytometry data assaying erythroctye binding, detected via the Alexa-Fluor 488 anti-C-tag nanobody, was performed in technical duplicate. SPR analysis of PfCSS-PfPTRAMP binding to PfRIPR was performed four times. Plasmodium experiments were replicated both through technical replicates and 3 independent biological replicates. All attempts showed similar results.
Randomization	As is standard for cryo-EM workflows, particles were split randomly into two halves and refined separately, as is automatically implemented in cryoSPARC. Randomization of other experiments was not relevant to this study as no subjective judgements were required about which data to include, exclude, or measure.
Blinding	The investigators were not blinded to the group allocation during the experiment and/or when assessing the outcome, as analysis were

Blinding	performed on quantitative endpoints that are not subject to investigator bias.

Reporting for specific materials, systems and methods

We require information from authors about some types of materials, experimental systems and methods used in many studies. Here, indicate whether each material, system or method listed is relevant to your study. If you are not sure if a list item applies to your research, read the appropriate section before selecting a response.

Materials & experimental systems

n/a	Involved in the study	
☐	☒	Antibodies
☐	☒	Eukaryotic cell lines
☒	☐	Palaeontology and archaeology
☒	☐	Animals and other organisms
☒	☐	Clinical data
☒	☐	Dual use research of concern

Methods

n/a	Involved in the study	
☒	☐	ChIP-seq
☐	☒	Flow cytometry
☒	☐	MRI-based neuroimaging

Antibodies

Antibodies used	- Rabbit anti-Rh5 (polyclonal, primary antibody). This is described in PMID: 22186897 and 3872115 and was validated using immunofluorescence and Western blotting against lines with and without PfRH5, as well as by growth-inhibition assays. - Rat anti-PfHSP70 (polyclonal, generated against recombinant P. falciparum HSP70 and described in 10.1126/sciadv.abe5396). Rat anti-PfHSP70 has been validated by western blot, using P. falciparum parasite lysates (10.1126/sciadv.abe5396). -Goat anti-Rat HRP (Sigma, A9037; secondary antibody) -Goat anti-rabbit HRP (BioRad, 172-1019; secondary antibody) -R5.004 and R5.011 (anti-PfRH5 monoclonal antibodies, PMID 31204103). These were validated by immunofluorescence, Western bot, protein crystallography and growth-inhibition of Plasmodium falciparum in human erythrocytes, as described in PMID 31204103. -Cy.003, Cy.004 and Cy.007 (anti-PfCyRPA monoclonal antibodies). These were validated in growth-inhibition assays and by protein crystallography in PMID 35177602. -Goat anti-Human IgG (H+L) Cross-Adsorbed AlexaFluor™ 488 Secondary Antibody (Invitrogen, A11013, secondary antibody) -CaptureSelect™ AlexaFluor™ 488 Anti-C-tag Conjugate (Thermo Scientific, 7213252100, nanobody)
Validation	Commercially available antibodies were validated by suppliers. Rabbit anti-RH5 has been characterized previously by IFA and immunoblot. Anti PfHSP70 rat antiserum was validated by immunoblot. R5.004, R5.011, Cy.003, Cy.004 and Cy.007 have been characterised by SPR and X-ray crystallography (PMIDs 31204103 and 35177602).

Eukaryotic cell lines

Policy information about cell lines and Sex and Gender in Research

Cell line source(s)	Commercial Freestyle™ 293-F cells (Thermo Fisher) and Expi293F™ cells (Thermo Fisher) were used for recombinant protein expression. Stable S2 cell lines for recombinant protein expression were generated in this study or reported previously (Hjerrild, K. A. et al. Production of full-length soluble Plasmodium falciparum RH5 protein vaccine using a Drosophila melanogaster Schneider 2 stable cell line system. Sci. Rep. 6, 30357 (2016); doi: 10.1038/srep30357). Native untransfected S2 cell lines are commercially available (ExpreS2ion Biotechnologies). Commercially available Sf9 insect cells (Thermo Fisher) were also used for recombinant protein expression. All Plasmodium cell lines are derived from P.falciparum 3D7, which is the first lab-adapted Plasmodium clone. The parasite clone originated from Dr David Walliker, Edinburgh University.
Authentication	Cell lines were not authenticated except for recombinant expression of the target protein. The first published Plasmodium falciparum genome (PMID: 12368864) is based on P. falciparum clone 3D7. We validated the 3D7 clone used by whole genome sequencing.
Mycoplasma contamination	All cell lines (Plasmodium and those used for recombinant expression) were not tested for mycoplasma contamination.
Commonly misidentified lines (See ICLAC register)	3D7 is the routinely used Plasmodium falciparum lab strain for which the first whole genome sequence was available; it is not listed in ICLAC.

Flow Cytometry

Plots

Confirm that:

☒ The axis labels state the marker and fluorochrome used (e.g. CD4-FITC).

☒ The axis scales are clearly visible. Include numbers along axes only for bottom left plot of group (a 'group' is an analysis of identical markers).

☒ All plots are contour plots with outliers or pseudocolor plots.

☒ A numerical value for number of cells or percentage (with statistics) is provided.

Methodology

Sample preparation	For measurement of parasitaemia: Parasitised and non-parasitised erythrocytes were fixed with 4% paraformaldehyde, 0.1% glutaraldehyde (Sigma) in PBS for 1 h at RT, followed by incubation for 1 h at 37°C with SYBR Green I (Life Technologies). Subsequently, 1µl of cells was resuspended in 2ml PBS prior to FACS readout. For erythrocyte binding assays: Red blood cells (O+ or O−) were washed twice in PBS containing 1% w/v bovine serum albumin (PBS/BSA), then 50 µl aliquots containing approximately 10 million cells were prepared. Following incubation with proteins for 1 hour at room temperature, cells were washed twice in PBS/BSA. To quantify the binding of PfRCR to erythrocytes, samples were stained in one of two ways as detailed below, then washed three times with PBS/BSA followed by dilution to approximately 6 million cells/ml before analysis. Staining procedure 1: to verify that the non-neutralising anti-PfRH5 antibody R5.011 could be used to quantify PfRCR binding to erythrocytes without impeding complex binding we first studied PfRCR labelled using the CaptureSelect™ AlexaFluor™ 488 Anti-C-tag Conjugate (7213252100, Thermo Scientific), incubated with cells for 1 hour at room temperature in the dark. Staining procedure 2: incubation with the monoclonal anti-PfRH5 antibody R5.011 as a primary antibody, followed by washing once, then incubation with a Goat anti-Human IgG (H+L) Cross-Adsorbed AlexaFluor™ 488 Secondary Antibody (A11013, Invitrogen). Primary and secondary antibodies were each used at 10 µg/ml in PBS/BSA for 1 hour at room temperature in the dark.
Instrument	BD LSR Fortessa X-20 Cell analyzer (for parasitaemia measurement) and Bio-Rad S3e Cell Sorter (for erythrocyte binding assays).
Software	To collect data, BD FACSDiva Software v9.0 (for parasitaemia measurement) and ProSort™ Software v1.6.0.12 (for erythrocyte binding assays) was used. Data were subsequently analysed using FlowJo v10.
Cell population abundance	For parasitaemia measurement: Thirty thousand singlet events for each sample. For erythrocyte binding assays: Fifty thousand events were recorded for each sample.
Gating strategy	For parasitaemia measurement: Gating for erythrocytes was achieved by plots of forward scatter area against side scatter area (gate = P1). Doublet discrimination required gating of forward scatter area against forward scatter width (gate = P2) followed by side scatter area against side scatter width (gate = P3). A SYBR Green-stained uninfected RBC sample was used as a negative control. Gating of SYBR Green positive, infected erythrocytes was achieved by plotting side scatter area against Alexa Fluor 488 area using 530/30 standard filter (gate = P4). Parasitaemia was determined by the number of cells identified in gate P4 as a percentage of those in gate P3. For erythrocyte binding assays: Erythrocytes were gated by plotting forward scatter area against side scatter area, then singlets identified by plotting forward scatter area against forward scatter height. Positively labelled erythrocytes corresponding to those with bound PfRCR were identified by plotting forward scatter area against Alexa-Fluor 488 area, with the positive gate placement guided by unstained red blood cells and those incubated with detection antibodies/nanobodies only. The number of positive cells is expressed as a percentage of the number of singlets recorded.

☒ Tick this box to confirm that a figure exemplifying the gating strategy is provided in the Supplementary Information.